Acid Transport Modeling Using Finite Element Discretization with

Weak Formulation for Simulation of Acid Fracturing

By

Mustafa Makki Al Hubail

Submitted to the graduate degree program in Chemical & Petroleum Engineering and the

Graduate Faculty of the University of Kansas in partial fulfillment of the requirements for

the degree of Master of Science.

Committee members:

_____

Chairperson: Dr. Barati, Reza

_____

Dr. Misra, Anil

_____

Dr. Vossoughi, Shapour

Date Defended: 05/09/2016

The Thesis Committee for Mustafa Makki Al Hubail

Certifies that this is the approved version of the following thesis:

Acid Transport Modeling Using Finite Element Discretization with

Weak Formulation for Simulation of Acid Fracturing

_____

Chairperson: Dr. Barati, Reza

Date Approved: 05/09/2016

Abstract

The purpose of designing an acid fracturing model is to examine the two factors that measure the effectiveness of the acid fracturing treatment. The two factors are the acid penetration distance and the fracture conductivity after closure stress is reached.

The acid fracturing model is designed by coupling a fracture propagation model and an acid transport model. The advanced fracture propagation models are developed numerically by the finite element method (FEM,) or the extended finite element method (XFEM.) However, the acid transport models that are reported in the literature are developed using the finite difference method (FDM.) The finite element method is a more stable and accurate technique to model different types of complex and coupled physics than FDM. Furthermore, FEM is a more powerful and suitable technique for meshing sophisticated geometries such as fractures. Thus, an acid transport model has been developed numerically using the finite element method.

The developed model solves the Navier-Stokes equations numerically to get the velocity profile. The acid balance equation is solved considering the convection and diffusion terms in all direction of the fracture and not only across the fracture. This model considers the thermal effect by solving the energy balance equation without neglecting the temperature gradient along the fracture length and height. The developed model predicts accurate acid penetration distance with a relative error of 0.3% compared to the analytical solution, and improves the predicted acid-etched width by more than 8% compared to the reported analytical solutions, which overestimate the acid-etched width because of no taking into account the effect of wormholes when calculating the total leak-off coefficient. Finally, the fracture conductivity, after fracture closure, has been estimated by using correlations.

Dedication

To my family.

Acknowledgment

Table of Contents

List of Figures

List of Tables

Chapter 1: Introduction

1.1 Acid Treatments

Acid treatments are stimulation techniques that are used to improve the production of oil and gas fields [1]. There are three different acid stimulation treatments. Acid wash, matrix acidizing and fracture acidizing [2]. Acid treatments are widely used because they have led to tremendous increase in the productivity of crude oil [1]. Acid treatments are mainly used in carbonate reservoirs, which make about 60% of the oil reserves in the world, and they hold many gas reserves as well [1]. It is believed that about 60% of the oil in the carbonate rocks is trapped due to several factors such as severe heterogeneity, and that percentage could reach up to 70% in heavy oil reservoirs; oil with API gravity values of 22 degree and below [1].

Acid wash is a treatment that is usually performed before the well is fully put into production where a small amount of acid is injected mainly to open the perforations and to remove any scale that is acid-soluble in the wellbore [2]. Matrix acidizing is a stimulation treatment in which acid is injected below the formation fracturing pressure, and the main purpose of this treatment is to remove any damage near the wellbore and to bypass the damage to create wormholes; hence, increase the oil and gas production [2]. Acid is also used in naturally fractured reservoirs in which the acid primarily flows through the natural fractures to generate more conductive paths for the fluid to flow in [3]. Finally, the acid fracturing treatment, which is the focus of this project, is going to be discussed in the next section.

For high permeability formations, the acid treatments are not practical because the acid will go to the high permeability zones and bypass the damaged low permeable zones. This would lead to early breakthrough of water or gas, or more production of water or gas from the high permeability zones [1]. Even if that does not occur, the incremental increase of oil and gas might not be worthy. Hence, designing an acid treatment is a crucial job and many factors must be considered such as the acid strength and the rock composition before bullheading, which is the term used when the acid is pumped through the casing or tubing [4]. Thus, selection of acid treatment zones must be considered wisely.

1.2 Acid Fracturing

Acid fracturing, which is the most common acid stimulation treatment in limestone and dolomite formations, is performed in two stages [2]. The first stage is the injection of a pad fluid, which is the term used to describe the front injected to adjust the temperature and salinity of the formation to make it more compatible with the acidic fluid and to start the fracture. The pad is injected at a pressure that is higher than the formation fracturing pressure. The pressure would build-up to a point that the formation cracks; hence, a hydraulic fracture is created, and it propagates as the injection continues [2]. The second stage is the injection of acid. Instead of using proppants as in conventional hydraulic fracturing to keep the fracture open, acid is injected above the formation fracturing pressure to keep the fracture open [4]. When the acid is injected, it non-uniformly etches the fracture surface; hence, a conductive pathway occurs after the fracture closes [5]. There are guidelines to determine whether acid fracturing or proppant fracturing is more practical for a certain formation [6]. Acid fracturing treatments are less complicated than proppant fracturing because there is no concern of proppant transport by fracturing fluids, and they

eliminate other issues such as proppant flow-back [5]. Furthermore, the acid fracturing could be the only available treatment to stimulate the well because the well might not be mechanically equipped to handle proppant [6]. On the other hand, proppant fracturing usually give a deeper penetration distance; hence, it is more favorable for extremely low permeability formation because longer fracture length is required to improve the production [6]. In addition, the cost of the proppant and the acid plays a major role in the designing stage. The cost of the acid is usually cheaper than the proppant; however, in certain cases, the cost of the acid exceeds the cost of proppant because the acid might require expensive additives that slow down the reaction rate to achieve a longer fracture length and an adequate acid etching width [4].

The acid, which is used in the acid fracturing treatment, is mostly hydrochloric acid, (HCl), with a concentration range of 15% to 28% [5]. The acid reacts on the fracture surface constantly as it travels along the fracture length, and the acid strength decreases as the acid etches the fracture surface [5]. When the concentration of the acid reaches 10% of the original concentration, it is said that the acid is spent, and it no longer has the capability to provide adequate etching to get satisfactory fracture conductivity [5].

1.3 Acid Fracturing Concepts

The main difference between an acid fracturing treatment and a hydraulic fracturing treatment is that acid is used in the acid fracturing treatment instead of proppant. The role of the acid in the treatment is to etch the rock surfaces, fracture faces, in a non-uniform manner so that the fracture stays open at the fracture closure pressure [5]. Hence, acid etching of the fracture faces is as important as the amount of the dissolved formation because if adequate amount of the formation was dissolved uniformly, the fracture would

completely close at the fracture closure stress; therefore, an acid fracturing treatment would work very well in heterogeneous formations [5]. The resulting fracture length and the fracture conductivity are the two main parameters that measure the effectiveness of an acid fracturing treatment [5].

Long fracture length is not a simple task to achieve because of acid leakoff and fast acid reaction with the formation. Many acid systems have been proposed to increase the fracture length, especially in high-pressure high-temperature (HPHT) formations [1] [5] [7]. HPHT formations are not the best candidates for the fracture acidizing treatment because at high temperatures the acid reacts rapidly with the formation; thus, the acid becomes spent, and it does not adequately penetrate the fracture. Every time the temperature increases 18° F, the acid reaction rate doubles; therefore, at high temperatures the acid-rock reaction rate increases [1] [7]. Therefore, high temperatures lead to short acid penetration distance [1] [7].

1.3.1 Acid Kinetics

It is important to have an idea about the distance the acid travels before it becomes spent while it penetrates the formation. The acid transfers to the formation by diffusion, convection, density gradient (free convection) or fluid loss [5]. The acid transfer rate is considered as the first step of acid kinetics. The second step is the reaction rate of acid once it reaches the fracture surface [5]. For strong acids such as HCl, the reaction goes to completion, which means there will not be a backward reaction rate constant, k_b, and this is the case in most applications in carbonate formations; thus, Eq. 1 represents the acid reaction rate expression.

$$r = k_f \, C_A^{\alpha} \qquad\qquad \textit{Eq. 1}$$

Where r is the reaction rate, k_f is the forward reaction constant, C_A is the acid concentration and α is the reaction order.

The reaction of acid on the rock surface is called surface reaction. A limestone formation has a high surface reaction rate whereas a dolomite formation has a much lower surface reaction rate [8]. Limestone has slow transfer of acid to the rock surface; thus, the acid-rock reaction kinetics of limestone is a mass transfer control kinetics [8]. For dolomite, when the fracture-face temperature is lower than 65 °C, the acid-rock reaction is mainly controlled by surface reaction; however, mass transfer controls the acid-rock reaction when the fracture-face temperature is higher than 93 °C [8]. When the temperature is between 65 °C and 93 °C, both surface reaction and mass transfer control the acid-rock reaction [8].

1.3.2 Acid Mass Transfer

The acid transfers to the formation by mainly two mechanisms. The first mechanism is diffusion, which occurs due to a concentration difference in two regions [8]. The acid transfers to the fracture surface and since the acid reacts with the calcareous rocks, there will be a concentration gradient; hence, the acid keeps traveling to the fracture surface as long as there is a concentration difference. The second mechanism is convection, which occurs due to pressure gradient [8] [5].

1.3.3 Thermal Effect

Reaction temperature plays an important role in acid fracturing treatments [9] [10]; yet, it is rarely considered in developing acid fracturing models. The acid temperature varies due to two main factors. The first factor is the exchange of heat with the formation,

and the second factor is the acid-rock reaction, which generates heat [5] [10]. The heat exchange could influence the mass transfer rate and the reaction rate [10]. Since the temperature is a key parameter in the acid reaction rate, the thermal effect has a significant role in the modeling of acid fracturing [10]. A change in the temperature could affect the amount of the spent acid; thus, the fracture length and the fracture conductivity will be effected, accordingly [10].

Acid fracturing is not a new stimulation technique; however, the industry lacks a complete model for the acid fracturing treatments, and that is due to several reasons [3]. One reason is that the acid fracturing treatment is very complex in its nature [3]. Various parameters should be considered to mimic the real treatment such as acid leak-off, formation heterogeneity and acid-rock reaction rate etc. Coupling all the parameters in one model makes the model very nonlinear, which leads to reason two. The second reason is computational limitation. It is impossible to have an analytical acid fracturing model that is complete. Hence, the only way to create a model that is close-enough to the real treatment is by creating it numerically. Therefore, computational limitation and computational time are barriers in achieving a complete acid fracturing model.

When a fracture propagation model and an acid transport model are coupled, they form an acid fracturing model [3]. The existing fracture propagation models, which are used for developing hydraulic fractures, are the same models that are used for acid fracturing models; thus, the acid fracturing simulators only differ in the acid transport model [3].

1.4 Objective

The main objective of this project is to create an acid transport model using finite element method (FEM.) FEM has not received enough attention in modeling computational fluid dynamics (CFD) problems because it requires more computational capabilities and more computational time than the finite difference method (FDM) and the finite volume method (FVM.) In addition, FEM might require stabilization technique to guarantee a conservative solution. However, FEM is more stable and more accurate technique for coupling complex physics, especially for viscous flow problems, than FDM and FVM [11].

In recent years, with the computational advances, FEM has been proven to be a more powerful and more suitable technique for meshing sophisticated geometries and dealing with complex 2D and 3D domains than FDM. This requires complex mapping and coordinate transformation to be implemented for complex geometries and that would complicate the governing partial differential equations (PDEs) even more [12]. Furthermore, the governing PDEs are directly addressed in FDM. This is not convenient compared to dealing with integral equations (weak forms) as in FEM. Moreover, the implementation of the boundary conditions is much easier in FEM, after generating the weak form, than in FDM [13]. Finally, most of the sophisticated fracture propagation models are developed using the finite element method, or the extended finite element method (XFEM).

To fully couple the two models that form the acid fracturing model, the fracture propagation model and the acid transport model, and since FEM is used in designing the sophisticated fracture propagation models, the acid transport model also is recommended

to be developed using FEM. Otherwise, there would be a gap between the propagation model and the acid transport model. Hence, in an attempt to close the gap, an acid transport model is going to be developed using FEM. The model is recommended to have these features:

1. The model must calculate the velocity profile inside the fracture by solving the Navier-Stokes equations.

2. The model is going to solve the acid balance equation to get the acid concentration profile considering the acid convection and diffusion in all direction and the acid reaction rate as a boundary condition.

3. The model solves the energy balance equation to get the temperature distribution inside the fracture.

4. The model must predict the acid penetration distance and the acid-etched width to calculate the final fracture conductivity by using correlations.

Outline of the objectives of this research is listed below:

1. A geometry that represents the fracture will be created, and it will be meshed, accordingly.

2. The weak forms of the governing partial differential equations are going to be generated.

3. The weak forms are going to be presented as kernels and coded in C++.

4. The finite element framework, Multiphysics Object-Oriented Simulation Environment (MOOSE) is going to be used to solve the system of the PDEs taking advantage of the already existing kernels.

5. The developed acid transport model is going to be validated versus the existing analytical and numerical models.

Chapter 2: Literature Review

Since the acid fracturing models use the same fracture propagation models as the models used for the hydraulic fracturing propagation models, a brief background of the hydraulic fracturing propagation models followed by a review of the acid transport models are reported in this chapter to comprehend the acid fracturing concept.

2.1 Hydraulic Fracturing Background

In Kansas, 1947, the first hydraulic fracturing treatment was conducted on a gas well in the Hugoton field [14]. Prior to that, in 1930s, Dow Chemical Company found that rock cracking and deformation occur when pressurized fluid is applied downhole and that would lead to an efficient matrix acidizing treatment [14]. In 1896, Herman Frasch had a US patent on matrix acidizing stating that if acid is injected under pressure, it goes further into the rocks and the oil flow increases [15].

A general definition of a hydraulic fracturing treatment is the process of initiating and propagating a fracture by a hydraulic load, which is created by the injected fluid [14]. There are many applications for hydraulic fracturing. For example, hydraulic fracturing is used to produce heat in geothermal reservoirs. For many decades, most of the research in hydraulic fracturing has been focused towards the oil and gas industry [14]. In the oil and gas industry, hydraulic fracturing is a stimulation technique that is greatly practiced these days to improve the production of low producing reservoirs. Hydraulic fracturing is the most common stimulation treatment; yet, modeling a hydraulic fracturing treatment is a very complicated process [14].

2.2 Modeling of Hydraulic Fracturing

Fractures occur perpendicular to the axis of the least principal stress [5] [4]. In most cases, the least stress is horizontal; thus, the fractures, in that case, would be vertical [5]. Since the least stress is horizontal, it is possible to create a fracture with pressure less than the overburden pressure [5]. The least principle stress is about one third of the effective overburden pressure [14]. The minimum required injection pressure to hold the fracture open or to extend it should be slightly more than the stress normal to the fracture and, as stated above, that injection pressure could be less than the overburden pressure if the fracture is vertical [14]. In-situ stresses variation, the formation-bed thickness, the rock properties and the pore pressure variation on different zones are factors affecting the propagation of a fracture [14].

Modeling of hydraulic fracturing requires coupling of three main processes. The first process is the rock deformation on the fracture surfaces by the pressurized fluid, crack-opening model [14]. The second process is the fluid flow inside the fracture [14]. The third process is the propagation of the fracture [14]. All of the processes must be coupled properly to achieve a proper solution. The theory of linear elasticity is used to model the crack-opening model [14]. The second process is modeled by relating the velocity of the fluid flow, the pressure gradient and the fracture width. The result of combining all the physics of the second process is a nonlinear partial differential equation [14]. The fracture propagation is modeled by the approach of linear elastic fracture mechanics theory, (LEFM) [14]. What makes the modeling process of hydraulic fracturing more complicated is that, in real life, fractures occur on different planes and different types of rocks, which have different properties, at the same time [14].

There are assumptions that are usually made for building a numerical hydraulic fracturing model. First, the reservoir material is linear elastic instead of poroelastic material. This assumption affects how the formation deforms and cracks [5]. The second assumption is that the fluid flow is Poiseuille flow, and it is incompressible [14]. In addition, the fluids are immiscible. The third one is that in multi-layer reservoirs, the layers are considered parallel and perfectly bonded [14]. Furthermore, it is assumed that the created fracture lies in one vertical plane [5]. There are other assumptions and simplification also made such as one-dimensional leak-off model [5].

The development of the theoretical hydraulic fracturing models was started in the 1950s. One of the models is the Perkins and Kern model, PK-model [16], which later became the famous (PKN) model when Nordgren added the effect of fluid loss to it [17]. Khristianovic, Geertsma and de Klerk developed the other famous model, which is called the (KGD) [18] [19]. The PKN model assumes that the fracture propagates in a vertical manner [20]. On the other hand, the KGD model assumes that the propagation occurs in a horizontal manner [20]. Refer to Figure 1 and Figure 2 for the PKN and KGD geometries, respectively. Both the PKN and KGD models are analytical two-dimensional models and the fluid flow is assumed to be only along the fracture [14]. Furthermore, the fracture height is assumed constant in both the models, and the changes are in the length or width of the geometry [20].

Due to the limitations of the 2D models, pseudo-3D models (P3D), planar 3D models (PL3D) and fully 3D models were developed [5] [14] [21] [22]. Table 1 provides a summary of the models. The new developed models intended to eliminate certain assumptions to make the model more realistic; assumptions such as constant fracture

height, perpendicular fracture orientation, one-dimensional fluid flow equation and how

the solution to the non-linear PDE for pressure-width is achieved [22] [21] [23].
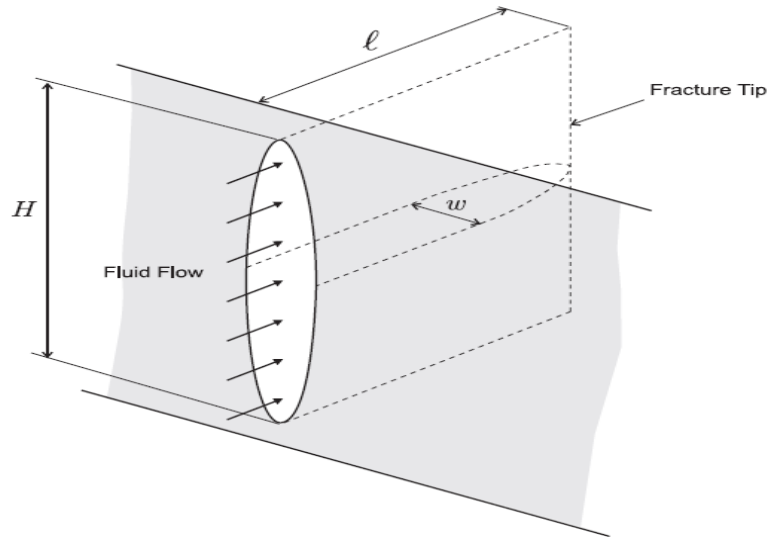
Figure 1: The PKN geometry (Adachi et al, 2007) [21]
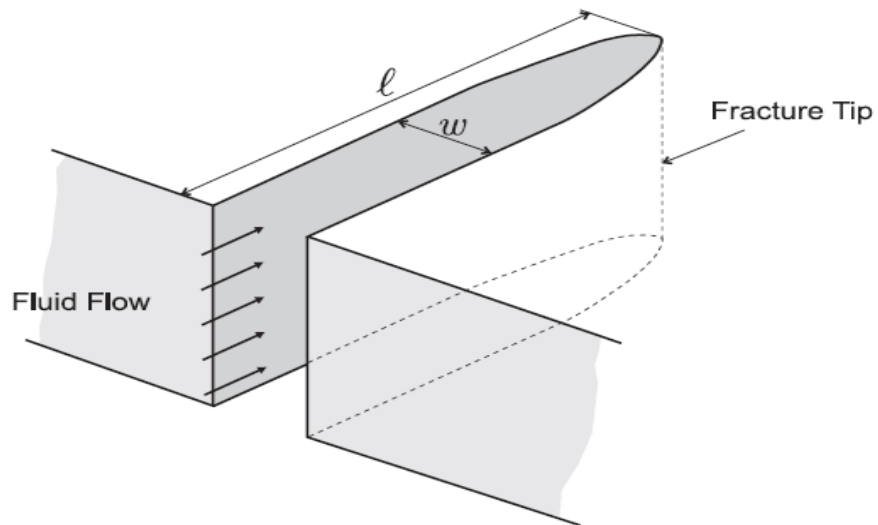
Figure 2: The KGD geometry (Adachi et al, 2007) [21]

Model	Fracture Orientation	Fracture Height	Flow Equation	Pressure-width Solution
PKN	Perpendicular	Constant	1D	Analytical
KGD	Perpendicular	Constant	1D	Analytical
P3D	perpendicular	Not constant	1D	Semi-Analytical
PL3D	Perpendicular	Not constant	2D	Numerical
Fully 3D	No assumption	Not constant	2D	Numerically intensive

2.3 Acid Transport Models

In 1972, Williams and Nierode started with the one-dimensional acid transport model as a set of equations, which are solved analytically, based on laboratory experiments [24]. They assumed infinite acid reaction rate, which means the concentration of the acid is zero at the fracture surfaces; thus, there is no acid reaction equation in the model [3]. Hence, acid mass transfer controls the model.

In 1975, Roberts and Guin modeled the acid transport as a two-dimensional model [25]. They considered the convection in the x-direction, along the length of the fracture, and the y-direction, the width of the fracture, but diffusion occurs only in the y-direction (Eq. 2) [25]. The diffusion term along the fracture length, x-direction, could be neglected because the acid flow along the fracture is dominated by convection. Convection dominates

the acid flow in the z-direction, the fracture height, too; hence, the diffusion term could also be neglected in the z-direction in the three-dimensional acid transport models [3]. Roberts and Guin also considered finite acid reaction rate [25]. Eq. 3 shows their acid reaction equation.

$$u \frac{\partial C}{\partial x} + v \frac{\partial C}{\partial y} = D_{eff} \frac{\partial^2 C}{\partial y^2}$$

<div align="right">*Eq. 2*</div>

$$-D_{eff} \frac{\partial C}{\partial y} = k_f C_i^n (1 - \varphi)$$

<div align="right">*Eq. 3*</div>

Where D_{eff} is the acid diffusion coefficient and φ is the formation porosity.

It was not until 1989 when Lo and Dean developed the first acid transport numerical model [26]. Their model was a steady-state model, and they assumed a constant leak-off rate [3]. In addition, their model requires averaged acid across the fracture width [3]. Furthermore, they assumed infinite acid reaction rate. Lo and Dean acid transport model is presented by Eq. 4 [26].

$$\frac{\partial C}{\partial x} = \left(\frac{2}{u\, w} \right) \left[-4.1 \left(\frac{D}{w} \right) + (0.37 v_l) - 0.01\, v_l^2 \left(\frac{w}{D} \right) \right] C$$

<div align="right">*Eq. 4*</div>

Settari developed a two-dimensional acid transport model in 1993 [10]. His acid transport model (refer to Eq. 5) is an unsteady-state model [10]. The model takes into account the acid mass transfer and the reaction rate [3]. Furthermore, the model considers thermal effects due to the heat of the reaction [10]. The fundamental problem with Settari's model is that it requires assuming average acid concentration across the fracture width and that leads to one-dimensional acid transport equation [3].

$$-\frac{\partial(u_x C)}{\partial x} - \frac{\partial(u_y C)}{\partial y} + \frac{\partial}{\partial y}\left(D_{eff}\frac{\partial C}{\partial y}\right) = \frac{\partial C}{\partial t} - q_{inj}\, C_{inj} \qquad \text{Eq. 5}$$

In 1998, Settari et al. were able to eliminate the need of averaging the acid concentration and the usage of the mass transfer coefficient by considering acid flow across the fracture, fracture width [27] [3]; however, their model is still a two-dimensional model.

Romero et al. developed a three-dimensional acid transport model in 1998 [28]. Eq. 6 presents the model. However, they had to use a technique to get the three-dimensional velocity profile from a two-dimensional velocity field [3]. Another limitation on the model is that it only considers uniform leak-off, and it does not consider the thermal effect [28].

$$-\frac{\partial(u_x C)}{\partial x} - \frac{\partial(u_y C)}{\partial y} - \frac{\partial(u_z C)}{\partial z} + \frac{\partial}{\partial y}\left(D_{eff}\frac{\partial C}{\partial y}\right) = \frac{\partial C}{\partial t} \qquad \text{Eq. 6}$$

The above models require assuming average acid concentration, using mass transfer coefficient or estimating the three-dimensional velocity profile from a two-dimensional velocity profile to get the acid concentration distribution because they are unable to compute the acid concentration profile across the fracture width. Hence, to eliminate the above requirements, the velocity profile must be calculated, and then the acid concentration distribution can be found using the velocity profile.

In 2009, Mou developed a three-dimensional acid transport model that uses the three-dimensional velocity profile by solving the Navier-Stokes equations using the SIMPEM method [3]. However, Mou's model is a steady-state model, and it assumes a Newtonian fluid. Furthermore, the model does not include the thermal effect [3].

In 2013, Oeth developed a three-dimensional acid transport model that is unsteady-state [29]. It considers the apparent viscosity to account for non-Newtonian fluids when

solving the Navier-Stokes equations in a pseudo-steady-state manner [29]. Oeth's model is an extension to Mou's model; hence, it does not account for the thermal effects [29].

Both Mou's model and Oeth's model are rigorous acid transport models; however, they do not consider the thermal effect, which plays a major role in the acid concentration profile [10]. Furthermore, the acid diffusion is only considered across the fracture. Moreover, the finite difference method was used in their models to solve the system of the PDEs numerically; hence, there would be a gap if sophisticated fracture propagation models, which are developed using FEM, were to be coupled with one of their models.

Chapter 3: Methodology of the Model Development

This chapter discusses the governing equations of the acid transport model, the steps required to derive the weak formulation and the development of the simulator in MOOSE.

3.1 The Governing Equations

The first step in modeling an acid transport is calculating the velocity profile inside the fracture. To do that, the Navier-Stokes equations are going to be solved.

3.1.1 The Navier-Stokes Equations

The Navier-Stokes equations are non-linear PDEs that represent the conservation of mass and momentum, and they govern the motion of fluids. In modeling of acid fracturing, the Navier-Stokes equations are the heart of the fluid flow model, specifically the acid transport model because they predict the velocity profile and the pressure distribution in a given geometry. Each term of the Navier-Stokes equations is a representation of a force balance; the forces are internal and external forces, pressure forces and viscous forces. For incompressible fluid, the Navier-Stokes equations are as follow.

The continuity equation, which is the mass balance equation for incompressible fluids (Eq. 7)

$$\left(\frac{\partial v_x}{\partial x} + \frac{\partial v_y}{\partial y} + \frac{\partial v_z}{\partial z} \right) = 0 \qquad \text{Eq. 7}$$

In compact form, this equation is written as:

$$\nabla . v = 0 \qquad \text{Eq. 8}$$

The momentum balance equations for incompressible fluids (Eq. 9 - Eq. 11) [30].

$$\rho\left(\frac{\partial v_x}{\partial t} + v_x\frac{\partial v_x}{\partial x} + v_y\frac{\partial v_x}{\partial y} + v_z\frac{\partial v_x}{\partial z}\right)$$
$$= -\frac{\partial P}{\partial x} - \left[\frac{\partial}{\partial x}\tau_{xx} + \frac{\partial}{\partial y}\tau_{yx} + \frac{\partial}{\partial z}\tau_{zx}\right]$$

$$\rho\left(\frac{\partial v_y}{\partial t} + v_x\frac{\partial v_y}{\partial x} + v_y\frac{\partial v_y}{\partial y} + v_z\frac{\partial v_y}{\partial z}\right)$$
$$= -\frac{\partial P}{\partial y} - \left[\frac{\partial}{\partial x}\tau_{xy} + \frac{\partial}{\partial y}\tau_{yy} + \frac{\partial}{\partial z}\tau_{zy}\right]$$

$$\rho\left(\frac{\partial v_z}{\partial t} + v_x\frac{\partial v_z}{\partial x} + v_y\frac{\partial v_z}{\partial y} + v_z\frac{\partial v_z}{\partial z}\right)$$
$$= -\frac{\partial P}{\partial z} - \left[\frac{\partial}{\partial x}\tau_{xz} + \frac{\partial}{\partial y}\tau_{yz} + \frac{\partial}{\partial z}\tau_{zz}\right]$$

Eq. 12 shows the N-S equation in a compact form, which is how it is codes in MOOSE.

$$\rho\frac{Dv}{Dt} = -\nabla P - [\nabla\tau]$$

Since most of the completion fluids in the industry follow a power law model, the shear stress for the power-law model is presented by Eq. 13 , and the shear rate is presented by Eq. 14:

$$\tau = K\,\dot{\theta}^n$$

$$\tau_{xy} = \eta\left(\frac{\partial v_y}{\partial x}\right)$$

Where K is the consistency index, θ is the shear rate, n is the power law index and η is the apparent viscosity.

Hence, Eq. 15 presents the apparent viscosity:

$$\eta = K\,\dot{\theta}^{n-1}$$

3.1.2 The Acid Balance Equation

The governing equation for the acid balance, which is required to get the acid concentration distribution inside the fracture at each time step, is a convection-diffusion PDE where the variable of interest is the acid concentration (C), and it is represented, in its compact form, by Eq. 16. For an acid transport model, the acid diffusion across the fracture is greatly larger than the other two directions [28]. Hence, the acid transport equation was simplified, in the literature models, by considering the acid diffusion only across the fracture as was shown in Eq. 2, Eq. 5 and Eq. 6. However, this is not the case in this model. The acid diffusion is going to be considered all over the fracture as can be seen in Eq. 16.

$$\frac{\partial C}{\partial t} = \nabla.(D\nabla C) - \vec{v}.\nabla C \qquad \text{Eq. 16}$$

3.1.3 The Energy Balance Equation

Since the thermal effect is going to be considered in this model, using the convection-conduction energy balance PDE is required to get the temperature distribution in the fracture. In the literature models, the thermal effect was rarely considered, and when it was considered, the assumption of the temperature gradient across the fracture is greatly larger than the other two directions was made. This is similar to the diffusion term in the acid transport equation. Hence, the energy balance equation was simplified to account for conduction only across the fracture [9]. In this model, the temperature conduction is going to be considered throughout the fracture as can be seen in the compact form of the energy balance equation (Eq. 17.)

$$\rho c_p \left(\frac{\partial T}{\partial t} + \vec{v}.\nabla T \right) = \nabla.(k_H \nabla T) \qquad \text{Eq. 17}$$

3.1.4 The Acid-Etched Width Equation

To measure how effective an acid fracturing treatment is, the fracture conductivity must be calculated. In order to calculate the fracture conductivity, the acid-etched width is calculated first. The acid-etched width equation is presented by Eq. 18. The acid type can be changed by modifying the gravimetric dissolving power and the molecular weight of the acid, accordingly.

$$\frac{\partial y}{\partial t} = \frac{\beta M_w}{\rho(1-\varphi)} \left(f_r v_l C_B - D \frac{\partial C}{\partial y} \right) \qquad \text{Eq. 18}$$

Where β is the acid dissolving power, M_w is molecular weight, ρ is acid density, v_l is leak-off velocity, f_r is the fraction of acid to react before leak-off, Cb is the acid concentration near the boundary and D is the acid diffusion coefficient.

Eq. 18 requires the leak-off velocity, v_l. The leak-off velocity, which is defined by Eq. 20, is going to be considered in this model by including the effect of wormholes.

3.1.5 The Leak-off Velocity

The leak-off velocity could significantly change the velocity field inside the fracture because the leak-off acts as a boundary condition in the Navier-Stokes equations. In most acid fracturing models, the leak-off velocity, which is presented by Eq. 19, is taken from the hydraulic fracturing models. A lower value for the leak-off velocity would predict longer fracture distance.

$$v_l = \frac{C_l}{\sqrt{t}} \qquad \text{Eq. 19}$$

Hill et al. studied one of the mechanisms that is different between proppant fracturing and acid fracturing, which is the effect of wormholes on the leak-off coefficient, C_l [31]. They found that the wormholes significantly affect the leak-off velocity. In fact, the effect could be more than 100% higher in limestone formations. Hence, modifying the leak-off velocity for acid fracturing treatments is necessary.

The study by Hill et al. found that the expression for the leak-off velocity (Eq. 19) does not change with wormholes; however, the total leak-off coefficient changes (Eq. 20) [31]. The total leak-off coefficient includes 1) the compressibility fluid-loss coefficient (Eq. 21,) and 2) the viscous fluid-loss coefficient (Eq. 22) [31]. Thus; to include the effect of wormholes in the model, the total leak-off coefficient; which is going to be a user input, should be considered to account for wormholes (Eq. 23.)

$$v_l = \frac{C_{wh}}{\sqrt{t}} \qquad\qquad \textit{Eq. 20}$$

$$C_c = \sqrt{\frac{\varphi k c_t}{\pi \mu}} \, (p_f - p_R) \qquad\qquad \textit{Eq. 21}$$

Where C_{wh} is the leak-off coefficient with wormholes, k is permeability, c_t is the total reservoir compressibility, μ is viscosity, P_f is the fracture pressure and P_R is reservoir pressure.

$$C_{v,wh} = \sqrt{\frac{\varphi k}{2\mu\left(1 - \frac{1}{Q_{ibt}}\right)}} \, (p_f - p_R)^{0.5} \qquad\qquad \textit{Eq. 22}$$

$$C_{wh} = \frac{-\frac{1}{C_c} + \sqrt{\frac{1}{C_c^2} + \frac{4}{C_{v,wh}^2}}}{2\left(\frac{1}{C_{v,wh}^2}\right)} \qquad\qquad \textit{Eq. 23}$$

3.1.6 Conductivity Correlations

After the acid-etched width is calculated, the fracture conductivity can be found using correlations. Correlations are developed either theoretically or empirically. The most famous and widely used fracture conductivity correlation is the Nierode-Kruk conductivity correlation, and it is an empirical correlation presented by (Eq. 24 - Eq. 28) [32] [33].

To be able to use the Nierode-Kruk correlation, first the ideal permeability (Eq. 24) and the ideal fracture conductivity (Eq. 25) must be calculated.

$$k_{fi} = \frac{w_i^2}{12} \qquad \text{Eq. 24}$$

$$\left(wk_f\right)_i = \frac{w_i^3}{12} \qquad \text{Eq. 25}$$

After that, the final fracture conductivity is calculated using Eq. 26.

$$wk_f = C_1 \exp(-C_2\sigma_c) \qquad \text{Eq. 26}$$

$$C_1 = 2.94 * 10^{-4} \left(wk_f\right)_i^{0.822} \qquad \text{Eq. 27}$$

$$C_2 = \begin{cases} (36.82 - 1.885 \ln(RES)) * 10^{-7} & 0 < RES < 1.38 \ * 10^8 \ Pa \\ (9.1 - 0.406 \ln(RES)) \ * 10^{-7} & 1.38 \ 10^8 \leq RES < 3.45 \ * 10^9 Pa \end{cases} \qquad \text{Eq. 28}$$

Where σ is the fracture closure stress, and RES is the rock embedment strength. All the above equations are derived based on SI units. Hence, the fracture conductivity would be in m³.

The theoretical models for the conductivity are infamous and rarely used because they require parameters that are related to the fracture etched surface, which cannot be

accurately obtained due to limited etching profile for the fracture surface [34] [35]. In recent years, researchers have developed new correlations by including geostatistical parameters when calculating the C_1 and C_2 coefficients of the Nierode-Kruk conductivity correlation [36]. What makes the Nierode-Kruk conductivity correlation widely used is its expedient because it does not need any assumptions of geostatistical parameters.

3.1.7 Boundary Conditions

This section presents the initial and boundary conditions that are going to be used in the model.

  I. Boundary conditions for the N-S equations:

➢ No slip conditions are applied at the top and the bottom of the fracture, z=0 and z=H (Eq. 29.)

$$v_x = v_y = v_z = 0 \hspace{4cm} \textit{Eq. 29}$$

➢ At the fracture tip, the fluid velocity is only in the x-direction, which is along the fracture (Eq. 30.)

$$v_y = v_z = 0 \hspace{4cm} \textit{Eq. 30}$$

➢ At the fracture surface, there exists leak-off including wormholes effect (Eq. 31.)

$$v_y = v_l \hspace{4cm} \textit{Eq. 31}$$

➢ At the fracture inlet, the flow enters the fracture only from the x-direction, and the injection rate is user specified (Eq. 32.)

$$v_{x=0} = v_i \qquad \text{Eq. 32}$$

II. Boundary conditions for the acid balance equation:

➤ At the fracture entrance, x=0, the acid concentration is the initial acid concentration, and it is user specified (Eq. 33.)

$$C(0, y, z) = C_i \qquad \text{Eq. 33}$$

➤ At the fracture surface, the boundary condition is the acid reaction rate (Eq. 34.)

$$D(\nabla C) = k\left(C_B - C_{eq}\right)^n (1 - \varphi) \qquad \text{Eq. 34}$$

III. Boundary conditions for the energy balance equation:

➤ At the fracture entrance, x=0, the temperature is the wellbore temperature (Eq. 35.)

$$T(x = 0, y, z, t) = T_i(t) \qquad \text{Eq. 35}$$

➤ Temperature far away from the fracture width is the reservoir temperature (Eq. 36.)

$$T(x, y \to \infty, z) = T_R \qquad \text{Eq. 36}$$

➤ Temperature at the fracture surface is the temperature of reservoir effected by the heat of the reaction (Eq. 37.)

$$k_H(\nabla T) = k_f C^\alpha (-\Delta H) + Q(t) \qquad \text{Eq. 37}$$

IV. Initial condition for the acid-etched equation:

➤ At time = 0, the fracture width is known (Eq. 38.)

$$y_{t=0} = y_i$$

Since the governing equations, the initial and boundary conditions and the conductivity correlation that represent the model are identified, the next step is to start the designing process.

3.2 The Model Workflow

All the above equations are going to be solved simultaneously for each time step providing the proper initial and boundary conditions. Figure 3 shows the required steps to model the acid transport using FEM.
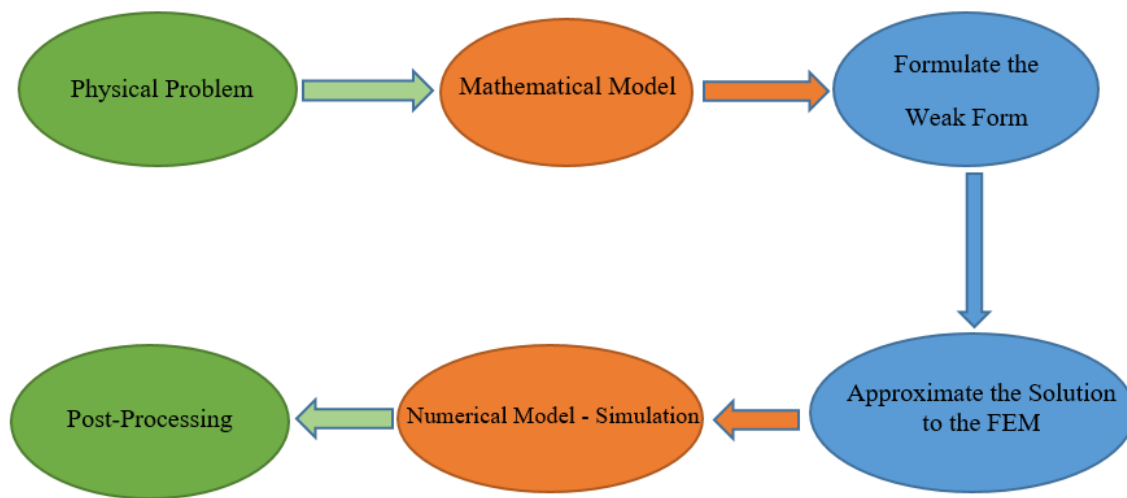
Figure 3: The modeling process

The mass balance, momentum balance, acid balance and the energy balance equations are going to be solved implicitly and in a transient mode. At each time step, the system of equations is solved. First, the velocity field is solved. The velocity field is then used to calculate the acid concentration and temperature distributions considering the acid reaction rate and the generated heat out of the reaction. This process is repeated for each time step until a specified tolerance is reached. After that, the acid-etched width is

26

calculated. This entire process is repeated until the final time step is reached where the fracture conductivity is calculated using the fracture conductivity correlation. The flowchart of the model is presented in Figure 4 and Appendix A.
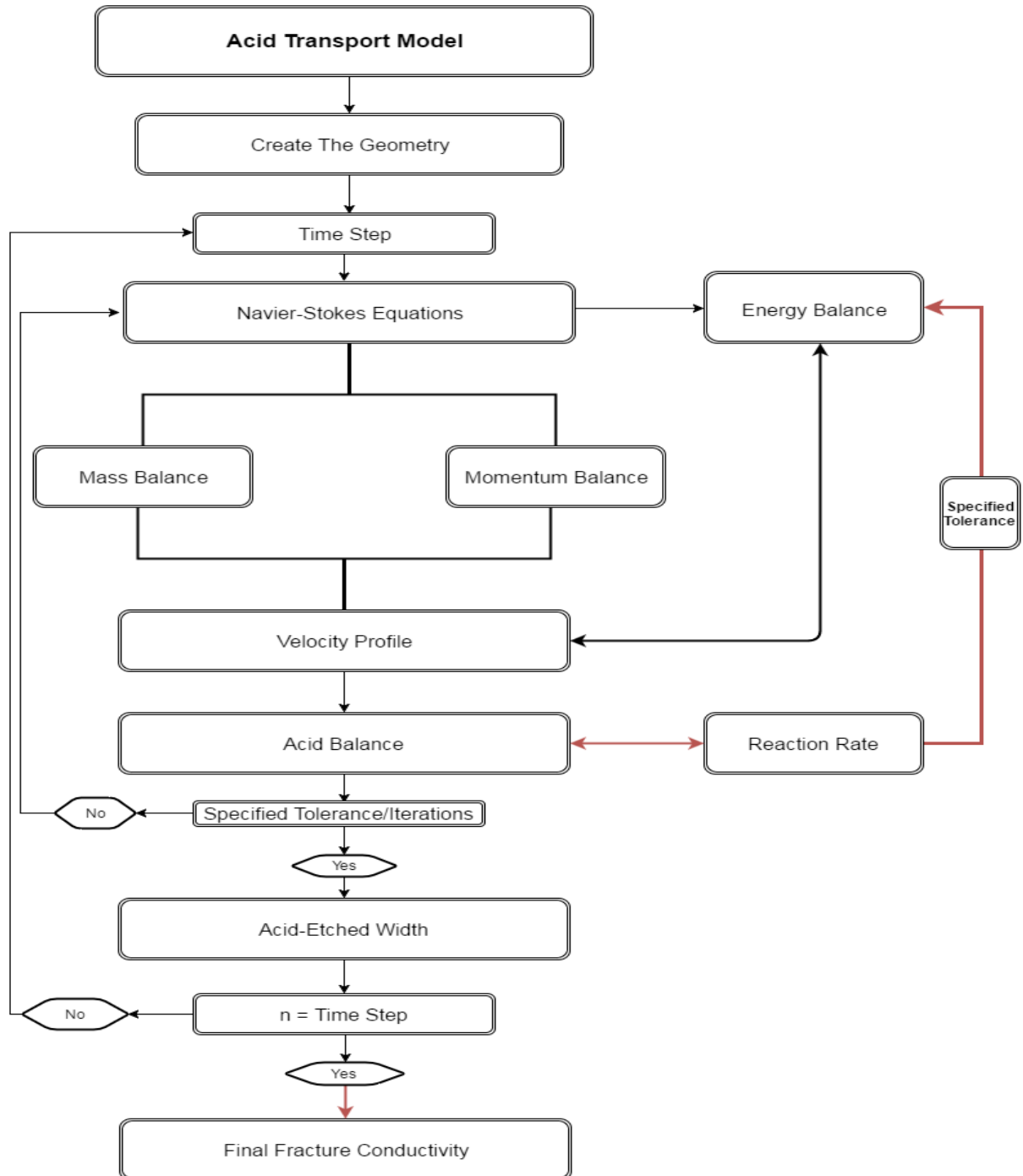
Figure 4: The flowchart of the model

3.3 Geometry Creation

The first step to build the simulator, as can be seen from the flowchart, Figure 32, is to create a geometry that represents the fracture using what is called a preprocessing software. The preprocessing software Trelis, which is provided by csimsoft, is going to be used to create the geometry before exporting it to MOOSE. Three essential tasks are performed in Trelis:

1- A computer-aided design (CAD) geometry is going to be created.

2- The geometry is going to be meshed in a manner to capture all the physics that are going to be simulated.

3- Blocks, sidesets and nodesets are going to be created to assign material properties and boundary conditions to the geometry.

The first task is to create a fracture. The created half-wing fracture geometry is based on a PKN model; which means the fracture propagates in a vertical manner, and the length and the height of the fracture are greatly larger than the width of the fracture (Figure 5.)

Figure 5: The created geometry

The second task is the meshing process. Meshing the geometry should be performed in a way that captures all the physics that need to be simulated to get accurate results. At the same time, it should be reasonable in regard of computational time. Quadrilaterals

elements with nine nodes (Quad9) are going to be used to mesh the fracture surfaces (Figure 6.)
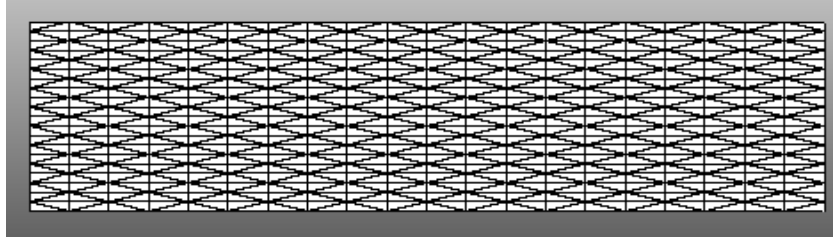
Figure 6: The meshed geometry

The third and the final task that needs to be performed in Trelis is to create blocks and sidesets. The creation of blocks and sidestes is a way to give "IDs" to a specific part of the geometry. This specific part of the geometry could be the entire volume of the geometry, a specific surface of the geometry, or perhaps just certain elements. Although all the three tasks are equally important and need to be performed very well, the creation of blocks and sidesets becomes the most crucial task of all for sophisticated geometries.

The importance of assigning the blocks and sidesets lies on the fact that neither material properties nor boundary conditions are assigned while creating the geometry in Trelis. The material properties and the boundary conditions are assigned within MOOSE. In MOOSE, one can assign different material properties for each block. For example, a geometry with two blocks; one block can be assigned specific material properties, permeability, porosity, Young's modulus, and the other block can be assigned the same values of porosity and Young's modulus, but different permeability values; hence, the result is a heterogeneous system. Similarly, the boundary conditions are assigned in MOOSE by using the created sidesets and nodesets. Each block is given an I.D. number so it can be identified later in MOOSE. The sidesets and nodesets are given ID numbers, too.

The created block and one of the nodesets for the geometry can be seen in Figure 7 and Figure 8, respectively. As can be seen in Figure 7, the whole fracture surface is selected as one block and given an I.D. number to assign the material properties to it in MOOSE. Figure 8 shows the created nodesets for the left boundary of the geometry, and it is given an I.D. number to assign the inlet boundary condition on it later in MOOSE.
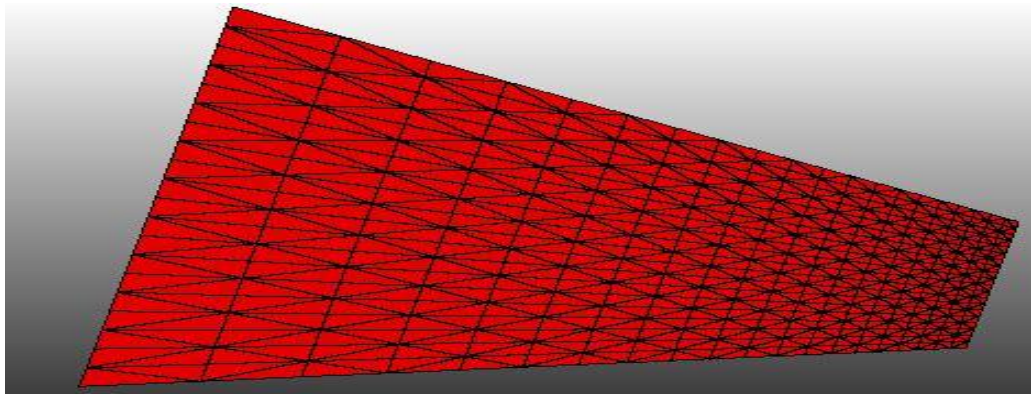
Figure 7: The created block
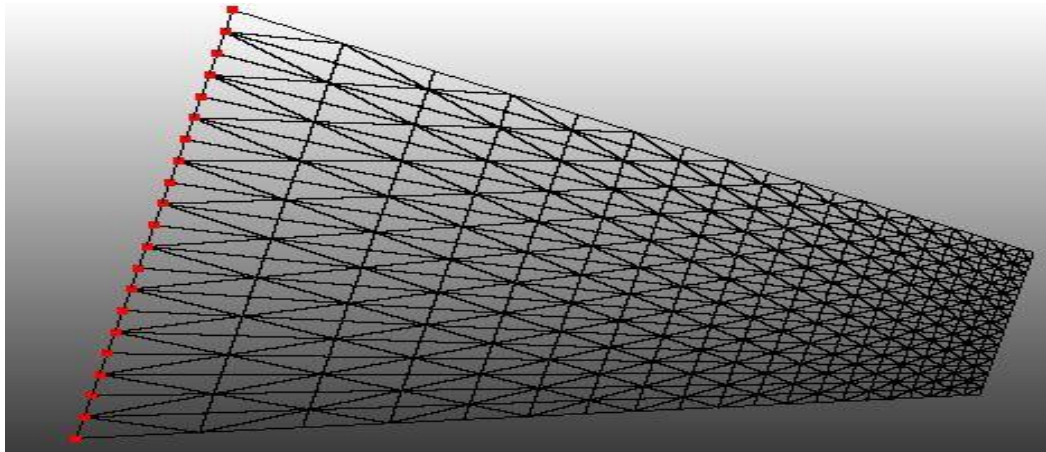
Figure 8: The created nodesets for the left boundary

3.4 The Generation of the Weak Formulation

Finite element method, which is a numerical method to approximate solutions for PDEs, is going to be used to solve the governing PDEs of the model. Here are the steps on how the FEM is going to be applied:

i.   The generation of the weak formulation for the governing PDEs is performed.

ii. The solution is approximated by the use of the shape/trial functions, (φ_j).

iii. The analytical integrals are converted to discrete summations.

iv. The set of the non-linear equations are solved by a solving mechanism such as the Newton's method.

3.4.1 Weak Form

The generation of the weak form is a mean to ease the process of finding a solution for ordinary or partial differential equations [12]. Solving the strong form of the governing differential equations is not always efficient. Furthermore, in some problems, a smooth solution for the strong form might not exist [13]. The weak form is a way to convert the differential equation to an integral equation; thus, an integral equation is solved conveniently instead of solving a differential equation [12]. Moreover, formulating a weak form makes the implementation of the boundary conditions relatively easy [12]. Because the weak form is more flexible than the strong form, the achieved solution from a weak form is called a weak solution.

The solution of the weak form, weak solution, is not perfectly accurate compared to the strong form solution because the requirements are reduced for the differential equations [13]. However, the weak solution gives very well results for engineering simulations. Therefore, most of the sophisticated simulator packages, such as Abaqus and

COMSOL are coded with a weak form algorithms. In addition, the MOOSE framework that is used to model the acid transport requires coded weak form kernels to solve a problem.

There are ways to increase the stability of the weak solution based on the type of the problem. For example, in elliptic differential problems, mesh refinement is sufficient to get accurate results. For fluid flow problems, preconditioning and stabilization techniques might be needed.

Generally the following steps are taken in order to generate the weak form:

   i.   The strong form of the PDE is written.

   ii. The terms of the PDE are rearranged making the right hand side of the equation to be zero.

   iii. The whole PDE is multiplied by a test function (ψ).

   iv. The whole PDE is integrated over the domain (Ω).

   v.   The PDE is integrated by parts using the divergence theorem to get the desired derivative order and at the same time generate the boundary integrals (BC).

The test functions should not be confused with the shape or trial functions. The shape/trial functions (φ_j) are the functions that are multiplied by coefficients and added up to form the approximated solution; hence, the shape functions are similar to the polynomial fitting functions. There are different types of shape functions, for example, linear Lagrange, quadratic Lagrange, and cubic Hermite. The test function depends on the type of the problem and the method to be used to solve the problem such as the Galerkin method. Yet, the test functions are the same as the shape/trial functions if the Galerkin finite element

method is used to represent the finite element solution. The Galerkin finite element method is going to be used in developing the acid transport model. It is applied by following the steps i to iv.

It is important to note that not all the terms of the PDEs should be integrated by parts (refer to step v) because the purpose of integrating by parts is to reduce differentiability and to generate boundary conditions that are physically meaningful [13]. Thus, it is essential to understand the problem at hand before generating the weak formulation.

Chapter 4: Numerical Analysis

This chapter shows the derivation of the weak formulation for the acid transport model, and discusses how the system of the non-linear equations are going to be coupled and solved using MOOSE.

4.1 Weak Form for the Navier-Stokes Equations

The Navier-Stokes equations are already developed in MOOSE; therefore, there is no need to derive the weak formulation for them. Table 2 shows the kernels that are going to be used for the acid transport model.

Table 2: The Navier-Stokes terms and kernels [37]

Term of Weak Form	Name of the Term	Name of the Kernel to be Used
$(\nabla . v)$	Mass balance	INSMASS
$\left(\rho \dfrac{\partial v}{\partial t}\right)$	Time derivative	INSMomentumTimeDerivative
$(\rho v . \nabla v)$	Convection	INSMomentum
$(-\rho \alpha \Delta v)$	Viscous	INSMomentum
(∇p)	Pressure	INSMomentum

The kernels in MOOSE are designed as a dimension independent physics; hence, even if the coordinate system is r and z, the same kernel can be used; however, the input file should be modified, accordingly [37].

4.2 Weak Form for the Acid Balance Equation

The steps to generate the weak formulation (refer to steps i - v) are going to be followed to generate the weak form for the acid balance equation.

❖ Start with the strong form of the acid balance equation, which is represented by Eq. 39.

$$\frac{\partial C}{\partial t} = \nabla.\,(D\nabla C) - \vec{v}.\,\nabla C \qquad\qquad \text{Eq. 39}$$

❖ The terms of Eq. 39 are rearranged to make the right hand side equal to zero:

$$\frac{\partial C}{\partial t} + \vec{v}.\,\nabla C - \nabla.\,(D\nabla C) = 0 \qquad\qquad \text{Eq. 40}$$

❖ Eq. 40 is multiplied by a test function, ψ_3, and integrated over the domain:

$$\int_\Omega \psi_3 \left\{ \frac{\partial C}{\partial t} + \vec{v}.\,\nabla C - \nabla.\,(D\nabla C) \right\} d\Omega = 0 \qquad\qquad \text{Eq. 41}$$

❖ Eq. 41 is integrated by parts to reduce differentiability and to generate the boundary condition.

$$\int_\Omega \left\{ \left(\psi_3 \frac{\partial C}{\partial t} \right) + (\psi_3 \vec{v}.\,\nabla C) + (\nabla \psi_3 (D\nabla C)) \right\} d\Omega$$
$$ - \oint_\Gamma (\psi_3 R_n)\, d\Gamma = 0 \qquad\qquad \text{Eq. 42}$$

❖ The boundary term of Eq. 42 is represented by Eq. 43:

$$R_n = D(\nabla C. \hat{n})$$

❖ The final weak form is represented by Eq. 44:

$$\int_\Omega \left\{\left(\psi_3 \frac{\partial C}{\partial t}\right) + (\psi_3 \vec{v}. \nabla C) + (\nabla \psi_3 (D \nabla C))\right\} d\Omega$$
$$- \oint_\Gamma D (\nabla C. \hat{n}) \psi_3 \ d\Gamma = 0$$

Each term including the boundary condition term in Eq. 44 is coded in MOOSE as a kernel similar to the Navier-Stokes terms as shown in Table 2.

4.3 Weak Form for the Energy Balance Equation

The weak form for the energy balance equation is generated the same way the acid transport equation was generated, and it is summarized in (Eq. 45 - Eq. 51.)

$$\rho c_p \left(\frac{\partial T}{\partial t} + \vec{v}. \nabla T\right) = \nabla. (k \nabla T)$$

$$\rho c_p \left(\frac{\partial T}{\partial t} + \vec{v}. \nabla T\right) - \nabla. (k \nabla T) = 0$$

$$\int_\Omega \psi_2 \left\{\rho c_p \left(\frac{\partial T}{\partial t} + \vec{v}. \nabla T\right) - \nabla. (k \nabla T)\right\} d\Omega = 0$$

$$\int_\Omega \left\{\left(\psi_2 \rho c_p \frac{\partial T}{\partial t}\right) + (\psi_2 \rho c_p (\vec{v}. \nabla T))\right.$$
$$\left. - (\psi_2 (\nabla. k \nabla T)) \right\} d\Omega = 0$$

$$\int_\Omega \left\{ \left(\psi_2 \rho c_p \frac{\partial T}{\partial t} \right) + \left(\psi_2 \rho c_p \, (\vec{v}.\nabla T) \right) + (\nabla \psi_2 . \mathrm{k} \nabla T) \right\} d\Omega$$
$$- \oint_\Gamma (\psi_2 q_n) \, d\Gamma = \; 0$$

Eq. 49

$$q_n = k(\nabla T . \hat{n})$$

Eq. 50

$$\int_\Omega \left\{ \left(\psi_2 \rho c_p \frac{\partial T}{\partial t} \right) + \left(\psi_2 \rho c_p \, (\vec{v}.\nabla T) \right) + (\nabla \psi_2 . \mathrm{k} \nabla T) \right\} d\Omega$$
$$- \oint_\Gamma k(\nabla T . \hat{n}) \psi_2 \, d\Gamma = \; 0$$

Eq. 51

4.4 Weak Form for the Acid-Etched Width Equation

The weak form for the acid-etched width is summarized in (Eq. 52 - Eq. 54.)

$$\frac{\partial y}{\partial t} = \frac{\beta M_w}{\rho(1-\varphi)} \left(f_r v_l C_B - D \frac{\partial C}{\partial y} \right)$$

Eq. 52

$$\frac{\partial y}{\partial t} - \left(\frac{\beta M_w}{\rho(1-\varphi)} \, f_r v_l C_B \right) + \left(\frac{\beta M_w}{\rho(1-\varphi)} D \frac{\partial C}{\partial y} \right) = 0$$

Eq. 53

$$\int_\Omega \psi_1 \left\{ \frac{\partial y}{\partial t} - \left(\frac{\beta M_w}{\rho(1-\varphi)} \, f_r v_l C_B \right) \right.$$
$$\left. + \left(\frac{\beta M_w}{\rho(1-\varphi)} D \frac{\partial C}{\partial y} \right) \right\} d\Omega = 0$$

Eq. 54

4.5 Finite Element Approximation

The system of equations are derived and coded in 3D; however, the model is going to be tested on a 2D geometry in order to compare the results with the existing models.

The next step is to approximate each variable that is going to be considered in the simulation (refer to step ii.) This step is called discretizing the weak form (refer to Eq. 55.)

$$C \approx C_e = \sum_{j=1}^{N} C_j \, \varphi_j \qquad\qquad \textit{Eq. 55}$$

Where φ_j is called the shape function. The shape function is a very critical piece in the finite element discretization as it plays an important role in the convergence criteria. For the 2D test, Table 3 shows each variable and its corresponding shape function order and type that are going to be used in the simulation. Since the Galerkin method is going to be used, the test functions and the shape functions share the same order and type.

Table 3: Shape functions

Variable name	Variable	Order	Type
Pressure	P	First	Lagrange
Velocity in x-direction	u	Second	Lagrange
Velocity in y-direction	v	Second	Lagrange
Temperature	T	Second	Lagrange
Acid concentration	C	Second	Lagrange

After discretizing the weak form, the next step is to convert the last analytical piece, which is the integral, to discrete sums using Gaussian Quadrature. By doing that, the final residual vector for Eq. 56 would end up in the form of Eq. 57:

$$\left(\nabla\psi_3 (D\nabla C)\right)$$

$$R_i(C_e) = \sum_{qp} \omega_{qp}\nabla\psi_i\left(x_{qp}\right).D\left(x_{qp}\right)\nabla C_e\left(x_{qp}\right)$$

The quadrature point position is x_{qp} and ω_{qp} is the associated weight. All the terms of the weak formulation of each equation are done the same way; hence, a nonlinear system of equations is achieved and the solution for the coefficients C_j, u_j, etc. for j = 1, …, N can be accomplished by using a proper solving mechanism such as the Newton's method.

$$R_i(C_e) = 0 \qquad i = 1, ..., N$$

$$R_i(v_e) = 0 \qquad i = 1, ..., N$$

$$.$$
$$.$$
$$.$$

Generating the weak formulation in kernels form is the essential task in order to use MOOSE. After that, the framework MOOSE takes care of all the tedious and repetitive work listed in this section. The coupling of the equations is done in the C++ kernel files and inside the input file. Figure 9 shows a small part of how the coupling is done for the acid balance equation. More can be found in Appendix D.

```
Acid::Acid(const InputParameters & parameters) :
  Kernel(parameters),

  // Coupled variables
  _u_vel(coupledValue("u")),
  _v_vel(_mesh.dimension() >= 2 ? coupledValue("v") : _zero),
  _w_vel(_mesh.dimension() == 3 ? coupledValue("w") : _zero),

  // Variable numberings
  _u_vel_var_number(coupled("u")),
  _v_vel_var_number(_mesh.dimension() >= 2 ? coupled("v") : libMesh::invalid_uint),
  _w_vel_var_number(_mesh.dimension() == 3 ? coupled("w") : libMesh::invalid_uint),
```

```
acid, space
[./C]
  type = Acid
  variable = C
  u = u
  v = v
[../]

acid, time
[./Acid_time]
  type = AcidTimeDerivative
  variable = C
[../]
```

Figure 9: The C++ and input file codes of the coupling of velocity components in acid balance equation

4.6 Model Validation

The developed model has to be validated with analytical solutions and existing numerical solutions before it becomes reliable.

4.6.1 Validation of Velocity Profile

To validate the velocity profile of the model, the analytical solution of laminar Newtonian fluid flow between two parallel plates is used (Eq. 58) [29].

$$u(y) = \frac{(p_{in} - p_L)\left(\frac{b}{2}\right)^2}{2L\mu}\left(1 - \left(\frac{y}{\frac{b}{2}}\right)^2\right) \qquad \text{Eq. 58}$$

Table 4 shows the data that is going to be used to test the model. Figure 10 shows that the velocity profile of the finite element model is very close to the analytical solution. Hence, the developed model can be used to predict acid penetration distance.

The difference between the analytical solution and the developed model when calculating the velocity profile is due to the leak-off velocity, which is not included in the analytical solution as can be seen in Eq. 58. Hence, when the leak-off velocity is a crucial component in the physical problem, the developed model is more accurate than the analytical solution.

Table 4: Simulation data to validate the velocity profile

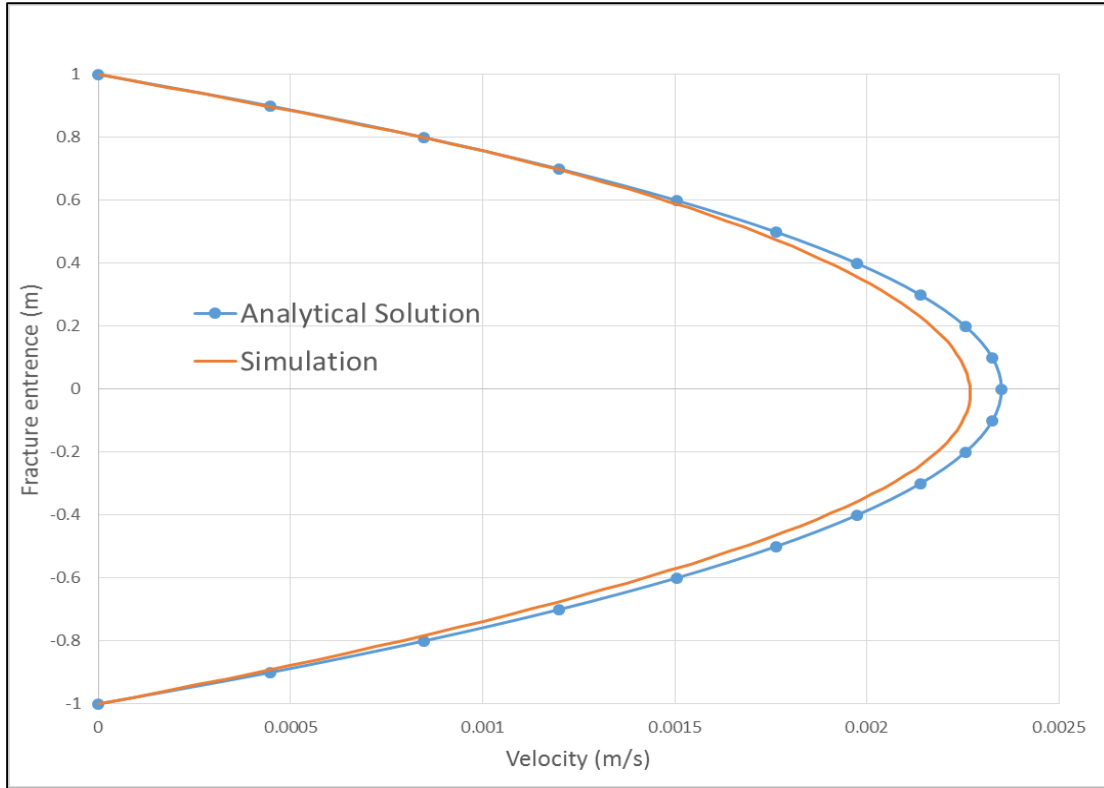| Length (m)	10
Viscosity (pa-s)	1
b, width (m)	2
Injection rate (bbl/min)	11.5
Reynolds number	15

Figure 10: The validated velocity profile against analytical solution (Eq. 58)

4.6.2 Validation of Acid Penetration Distance

Since the velocity profile was validated with the analytical solution, the acid penetration distance can be predicted. The next step is to validate the acid balance model.

In early designs of acid fracturing models, as an analytical practice, the Peclet number is used to predict the acid penetration distance [33]. Schechter experimented with different Peclet numbers, and plotted the results of the dimensionless average acid concentration vs. the dimensionless acid penetration distance (Figure 11) [33]. The Peclet number is calculated using Eq. 59.

$$N_{pe} = \frac{\overline{v_l} w}{2 D_{eff}} \qquad\qquad \textit{Eq. 59}$$
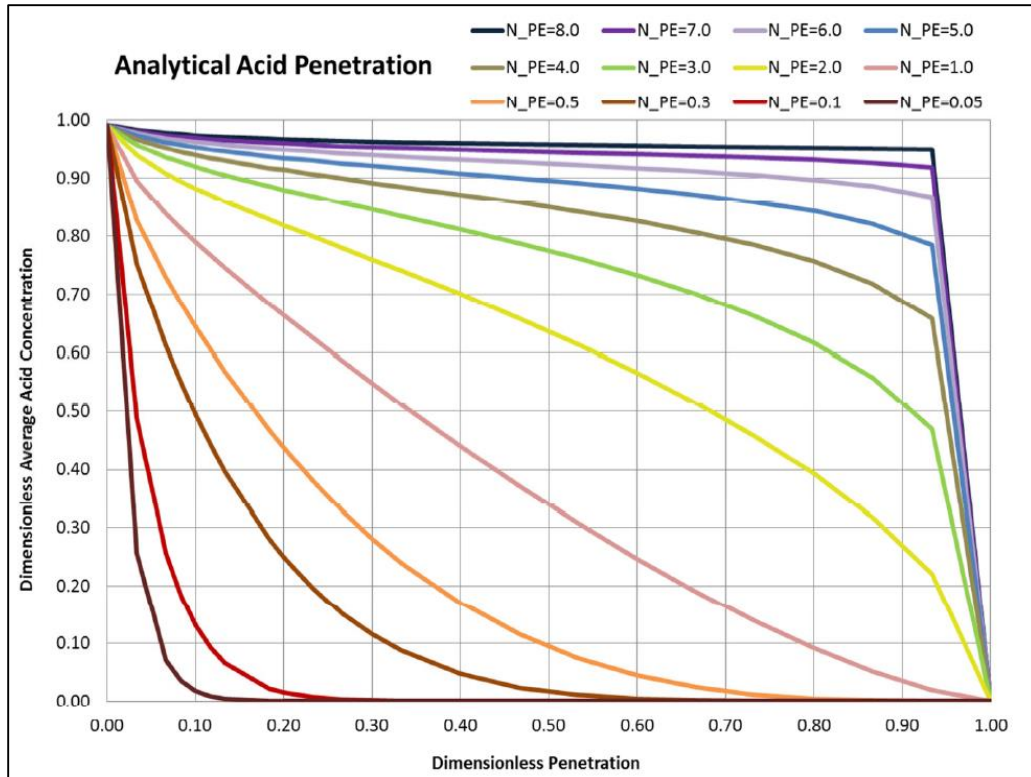
Figure 11: Analytical acid penetration distance [33] [29]

From Figure 11, the dimensionless acid penetration distance can be predicted by knowing the Peclet number and the dimensionless average acid concentration. Likewise, knowing the Peclet number and the dimensionless acid penetration distance, Figure 11 can be used to find the dimensionless average acid concentration.

By running the simulator with a specific Peclet number, the acid penetration distance is predicted. Then, by exporting the output file from MOOSE to a post-processing software such as ParaView, the acid concentration at each node of the geometry can be found; hence, the average acid concentration inside the fracture can be calculated. Thus, a comparison between the simulation and the analytical results can be conducted. Table 5 shows the data that is used to do the comparison between the simulator and the analytical solution (Figure 11.) Table 6 shows the simulation results.

Peclet number	4
Leak-off velocity (m/s)	0.0004
Stimulation time (s)	3600
Leak-off coefficient (m/$\sqrt{s}$)	0.024
Width (mm)	2
Diffusion coefficient (m^2/s)	0.0001

Table 6: Simulation results validating the acid penetration distance

Acid penetration distance (m)	9.68
Average concentration (%)	5.68
Dimensionless penetration	0.968
Dimensionless average concentration	0.3787

For a Peclet number of 4, and a dimensionless average acid concentration of 0.378, Figure 11 gives a dimensionless acid penetration of 0.965 whereas the simulation gave a dimensionless acid penetration of 0.968. Thus, the relative error is approximately 0.3%.

4.6.3 Validation of Acid-Etched Width

In order to find the fracture conductivity, which is the second factor that measures the effectiveness of an acid fracturing treatment, the acid-etched width must be calculated first.

Figure 12 shows the analytical solution for the acid-etched width at different Peclet numbers [33].
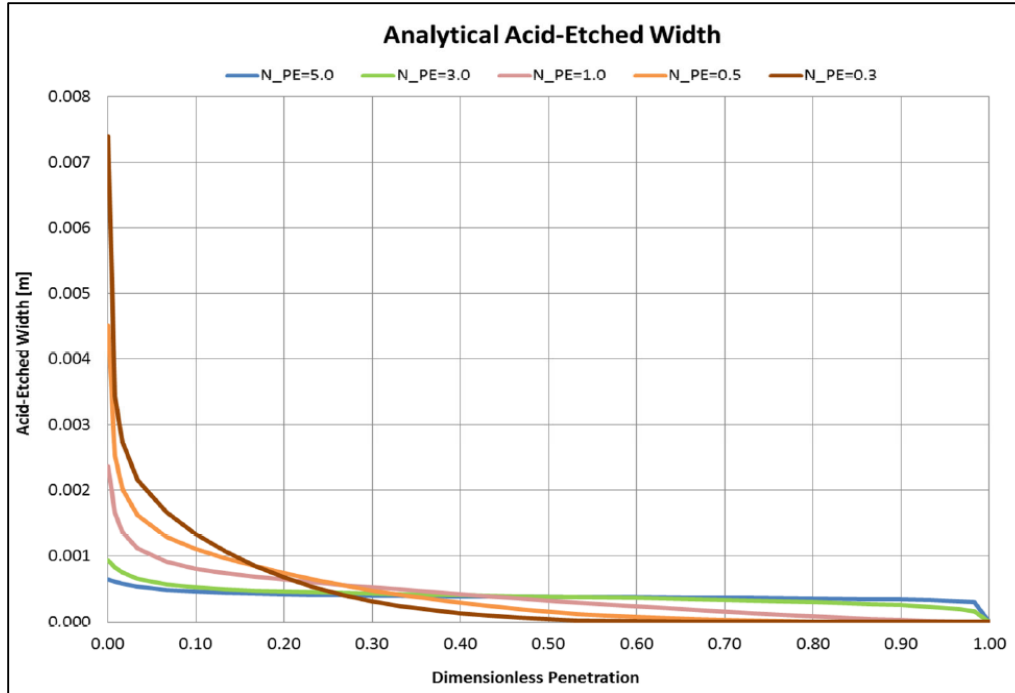
Figure 12: Analytical acid-etched width [33] [29]

Table 7 shows the data that is going to be used in the simulator to validate the acid-etched width.

Table 7: Simulation data to validate acid-etched width (Schechter, 1992)

Gravitational dissolving power, kg/kg acid	1.37
Acid molecular weight	36.46
Acid density, kg/m^3	1000
Porosity	0.15
Fraction of acid to react before leak-off	0.7
Average acid concentration, %	5.68
Diffusion coefficient, m^2/s	0.0001
Acid concentration at boundary %	15

For a Peclet number of 4, and a dimensionless acid penetration distance of 0.968, Figure 12 gives an acid-etched width of 0.233 (mm). The simulator gives an acid-etched width of 0.214 (mm). However, the simulator takes into account the effect of wormholes,

which is not included in the analytical solution, and that is why the simulator gave a narrower acid-etched width than the analytical solution; hence, the analytical solution overestimates the acid-etched width. If the effect of wormholes on the total leak-off coefficient is neglected, the simulator would give an acid-etched width of 0.2338 (mm); hence, the relative error between the analytical solution and the simulator is 0.34%. Including the effect of wormholes when calculating the leak-off coefficient actually makes the model more realistic; therefore, this model improves the result of the acid-etched width by 8.1%.

4.6.4 Validation of Temperature Distribution

The model's temperature distribution is going to be validated against Settari's model because it considers the thermal effect [10]. Table 8 shows the data for this test, and the result can be seen in Figure 13 and Appendix B.

As can be seen in Figure 13, the simulation results are in good agreement with Settari's model. The maximum difference between the simulation and Settari's model is approximately 3.5 ºC, and the relative error ranges between 0.7% and 4.4%.

Table 8: Simulation data to validate the temperature distribution (Settari, 1993)

| Data	value	unit
Injection rate	20	bbl/min
Treatment volume	200	STB
Viscosity	0.1	Pa-s
Acid Density	1000	kg/m^3
Thermal conductivity	0.584	Watts/m-C
Specific heat	4.179	KJ/Kg-C
Diffusivity coefficient	0.0001	m^2/s
Temperature reference	60	^oC
Reaction order	0.441	
Reaction constant	$4.129 * 10^{-4}$	cm/s
Heat of reaction (enthalpy)	1090	KJ/Kg
Initial acid concentration	28	%
Leak-off coefficient	0.0006	$m/s^{0.5}$
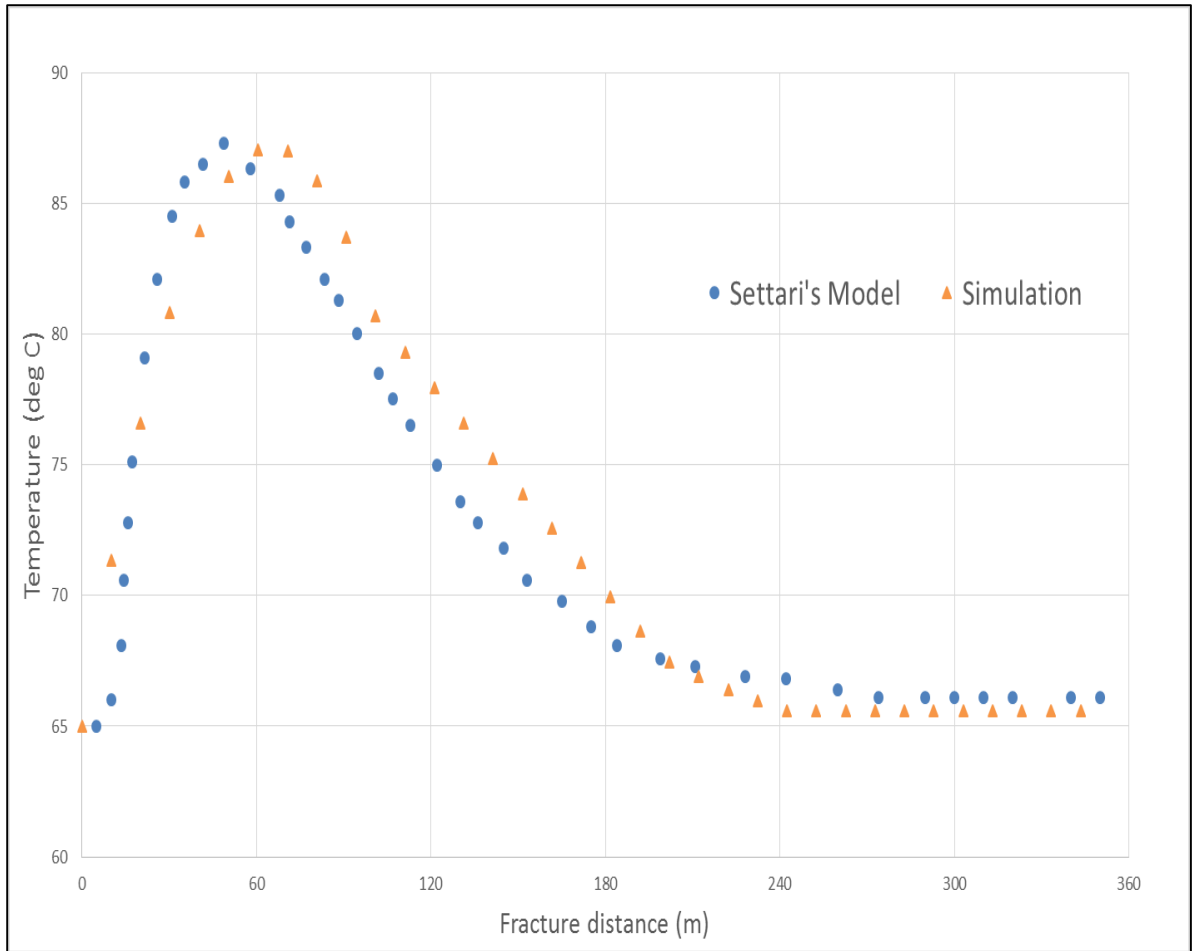
Figure 13: The validated temperature profile vs. Settari's model

Chapter 5: Results and Discussion

After validating the model with analytical solution, it can be used to study the effect of different parameters on the acid transport model.

5.1 Influence of Non-Newtonian Fluids on Acid Penetration Distance

The model can be used to simulate non-Newtonian fluids after the appropriate kernels and material properties have been added; hence, a comparison between Newtonian and non-Newtonian fluids can be made. First, the shear stress and shear rate relationship should be presented to detect the type of the non-Newtonian fluid. In addition, the apparent viscosity curve is shown to see how the power law fluid is behaving. The velocity profile for the Newtonian and non-Newtonian fluids is plotted to clearly capture the effect of the power law fluid. Finally, a comparison between Newtonian fluids and non-Newtonian fluids is conducted to see how they affect the acid travel distance inside the fracture. Table 9 shows the data used for the power law fluid.

Table 9: Simulation data for a non-Newtonian fluid

Consistency index (kg/m.s2-n)	0.3
power law index	0.55

Figure 14 shows the relationship between the shear stress and the shear rate for the Newtonian and the non-Newtonian fluid. It is clear that a straight line is achieved for the Newtonian fluid whereas the non-Newtonian fluid behaves as a pseudo-plastic fluid.

Figure 15 and Figure 16 show the relationship between the apparent viscosity and the shear rate for the two different fluids.
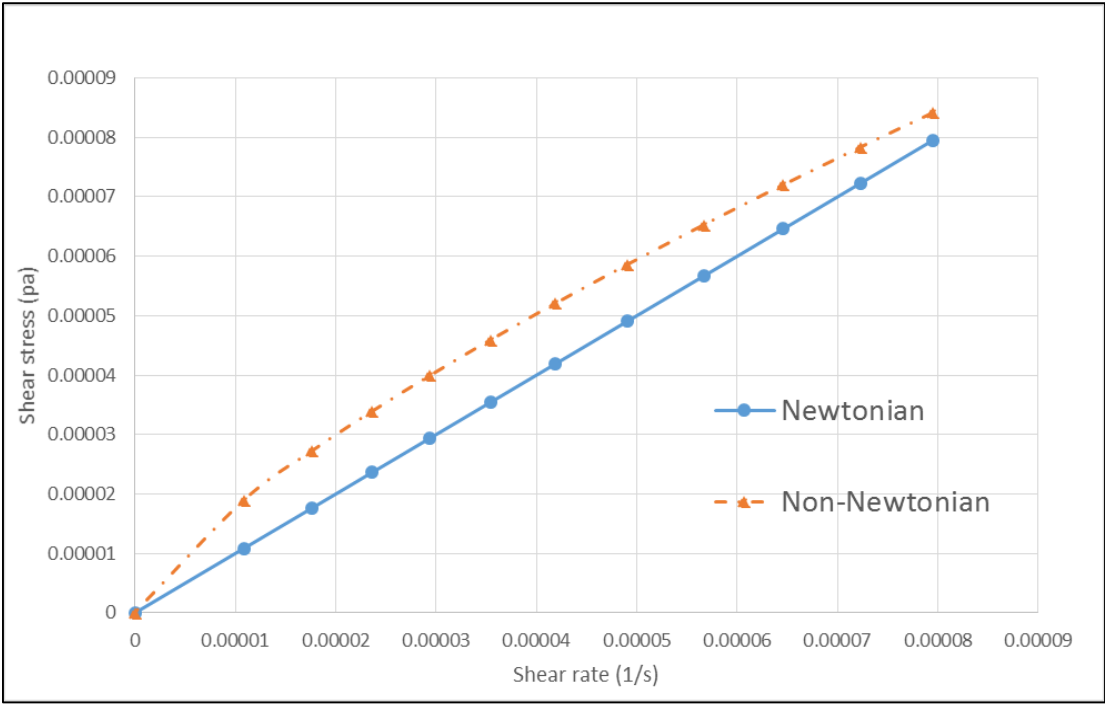
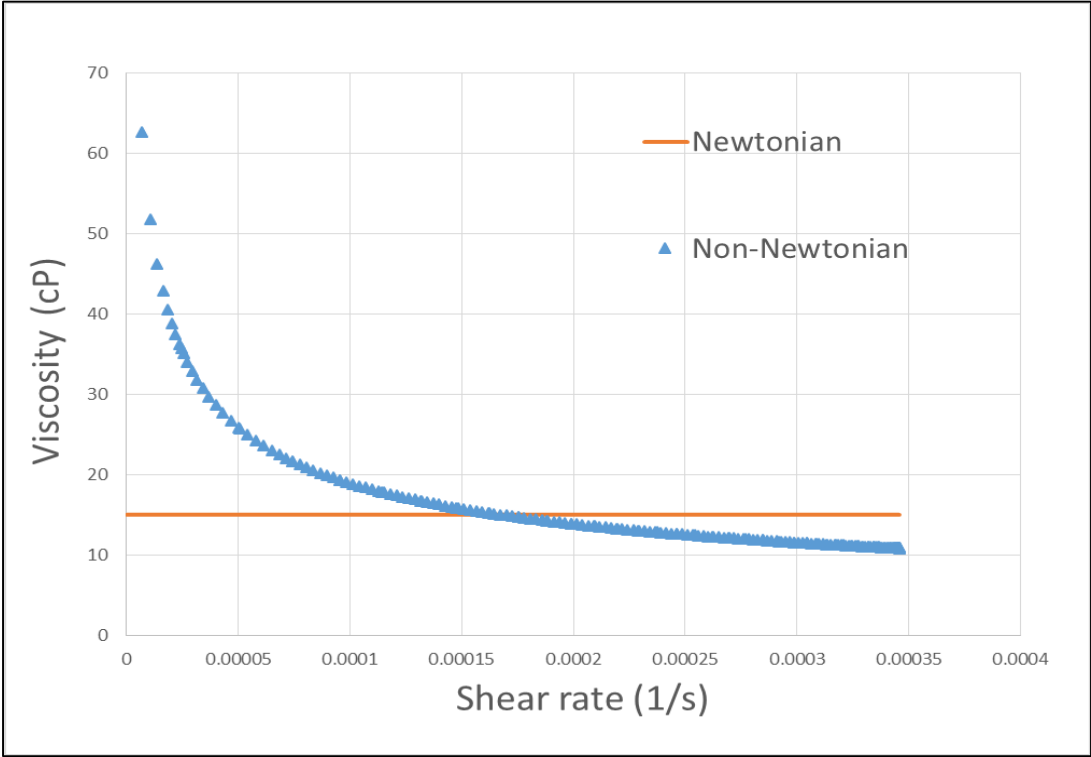*Figure 14: The relationship of shear stress & shear rate*

Figure 15: The viscosity curve for Newtonian vs. non-Newtonian fluids

By plotting the apparent viscosity and the shear rate on a log-log scale, Figure 16 clearly shows the power law region.

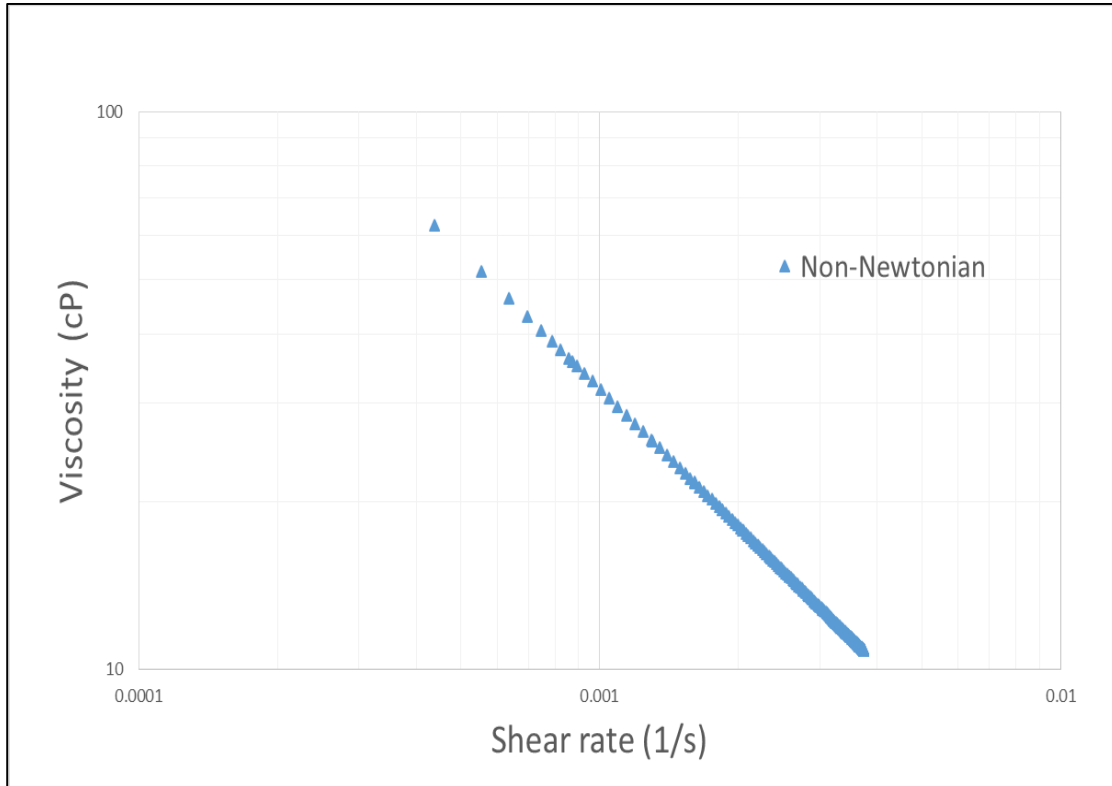*Figure 16: Apparent viscosity curve for the non-Newtonian fluid*

The effect of the apparent viscosity on the velocity profile is shown in Figure 17 and the effect on the acid penetration distance is shown in Figure 18.

Not only the acids behave as non-Newtonian fluids; however, the fracturing fluids behave as viscoelastic surfactant fluids as well, and this affects the generation of the fracture [38] [39].
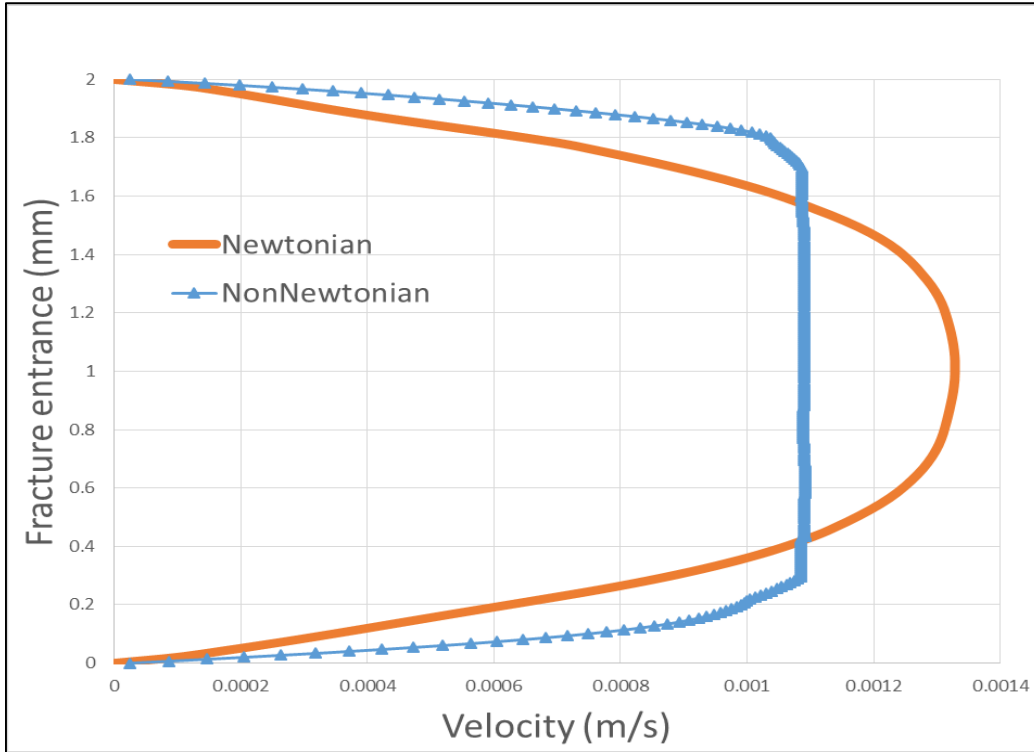
Figure 17: The comparison of velocity profile for Newtonian and non-Newtonian fluids
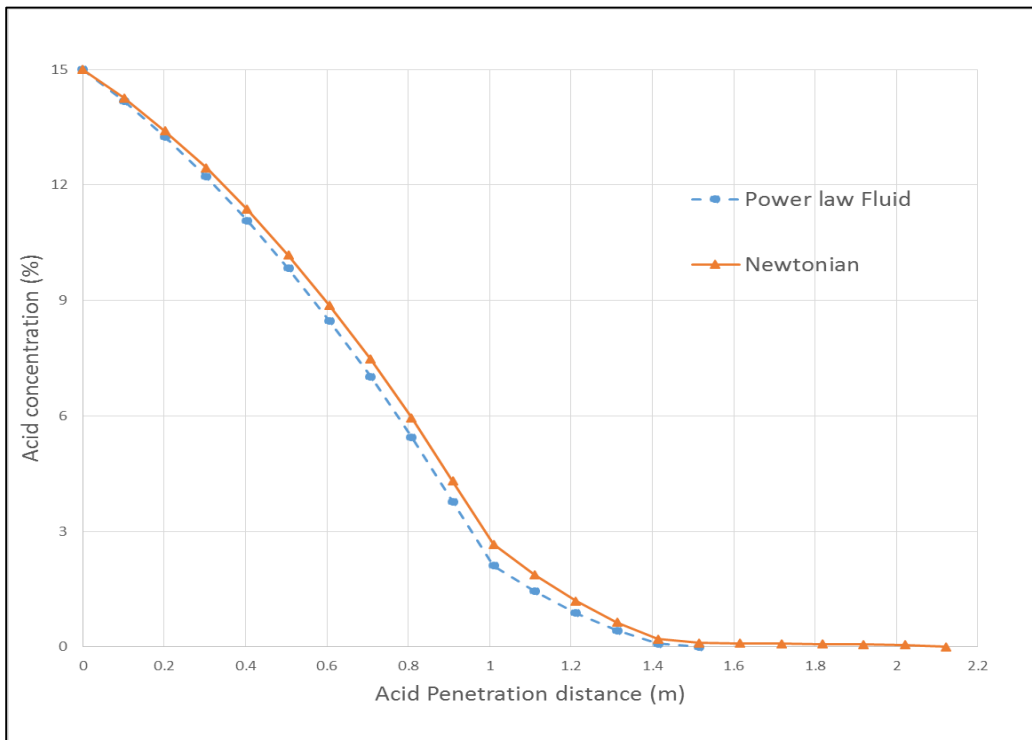

Figure 18: The comparison of acid penetration distance between Newtonian and non-Newtonian fluids

Figure 18 shows that the acid that acts like a Newtonian fluid tends to travel a slightly longer distance inside the fracture before it becomes spent.

5.2 Influence of Viscosity on Acid Penetration Distance

Two main factors measure how successful an acid fracturing treatment is. The first one is the acid penetration distance. The second parameter is the fracture conductivity. The model is going to be used to see how the acid viscosity affects the acid penetration distance inside the fracture. Then, different acid concentrations are going to be used in the simulator to see which parameter, the acid concentration or the acid viscosity, has a more significant role in the acid penetration distance while fixing the other parameters.

Figure 19 shows that the higher the viscosity of the acid the longer the acid penetration distance; hence, viscous acid performs better than straight acid.
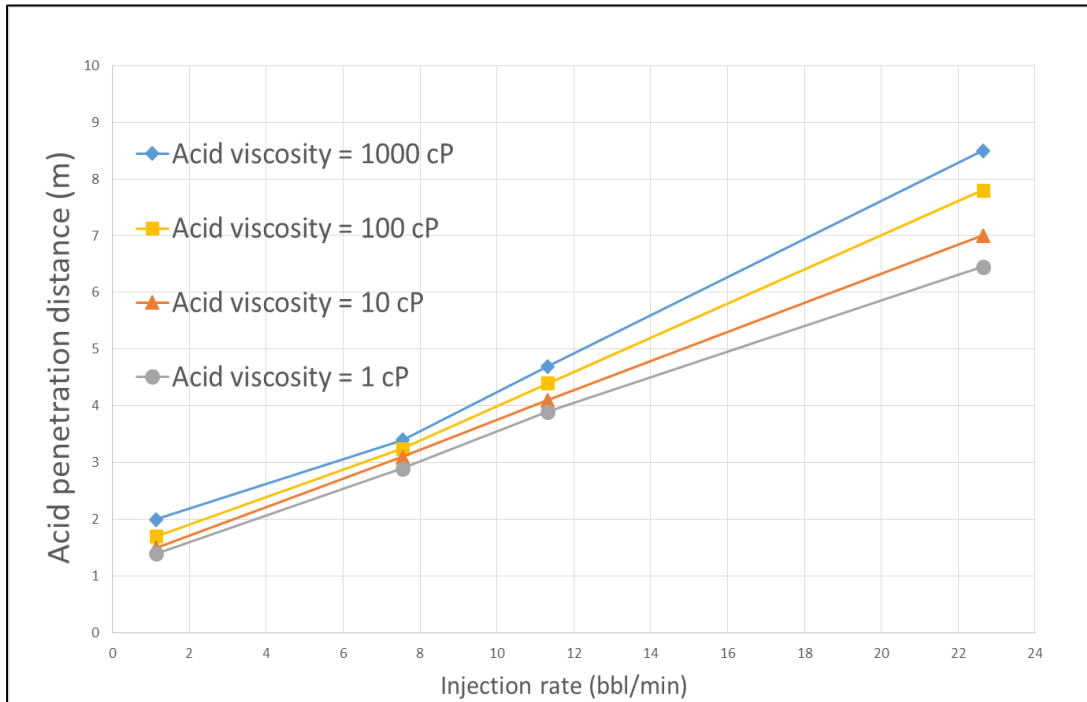

Figure 19: The effect of the viscosity on acid penetration distance after 30 minutes of stimulation

Figure 20 shows that acid with high viscosity tends to penetrate the fracture much better than acid with high concentrations. The effect of different acid concentrations on the fracture conductivity can be seen in Figure 28 and Figure 29.
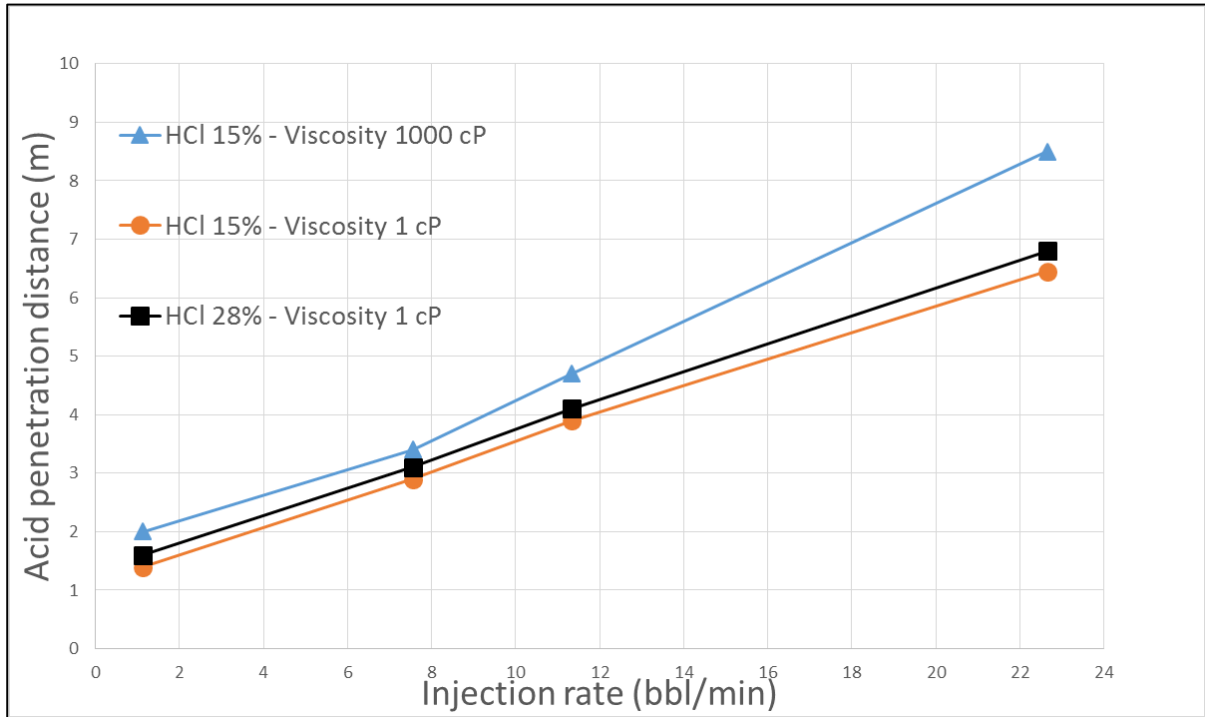
Figure 20: The effect of high acid concentrations vs. high acid viscosity after 30 minutes of stimulation

5.3 Acid Penetration and Acid-Etched Width effect on Fracture Conductivity

Figure 21 shows the relationship between the acid-etched width and the acid penetration distance. It is clear from Figure 21 that more etching occurs near the fracture entrance, which is closer to the wellbore. The acid-etched width gets narrower with longer acid penetration distance because the acid becomes spent; hence, the dissolving power of the acid decreases.

Figure 22 and Figure 23 show the fracture conductivity after the fracture closure is reached. It is obvious that wider etched-width would give higher fracture conductivity,

which occurs near the fracture entrance. The fracture conductivity gets smaller as the fracture length increases as can be seen in Figure 22.
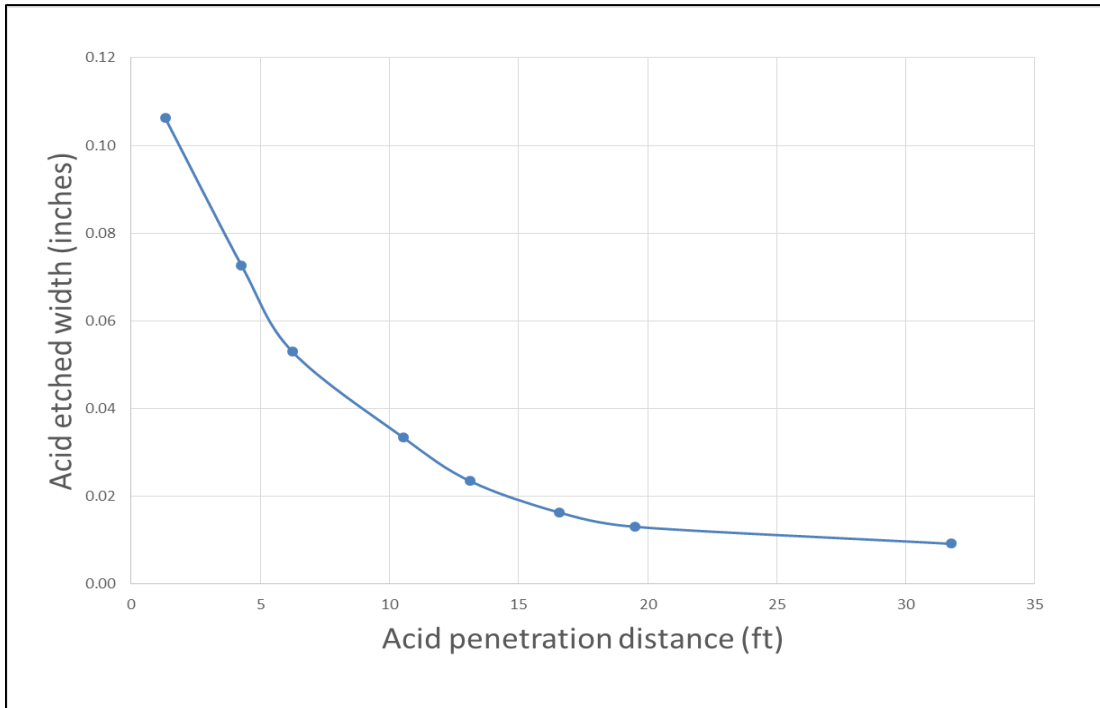
Figure 21: Acid-etched width vs. acid penetration distance
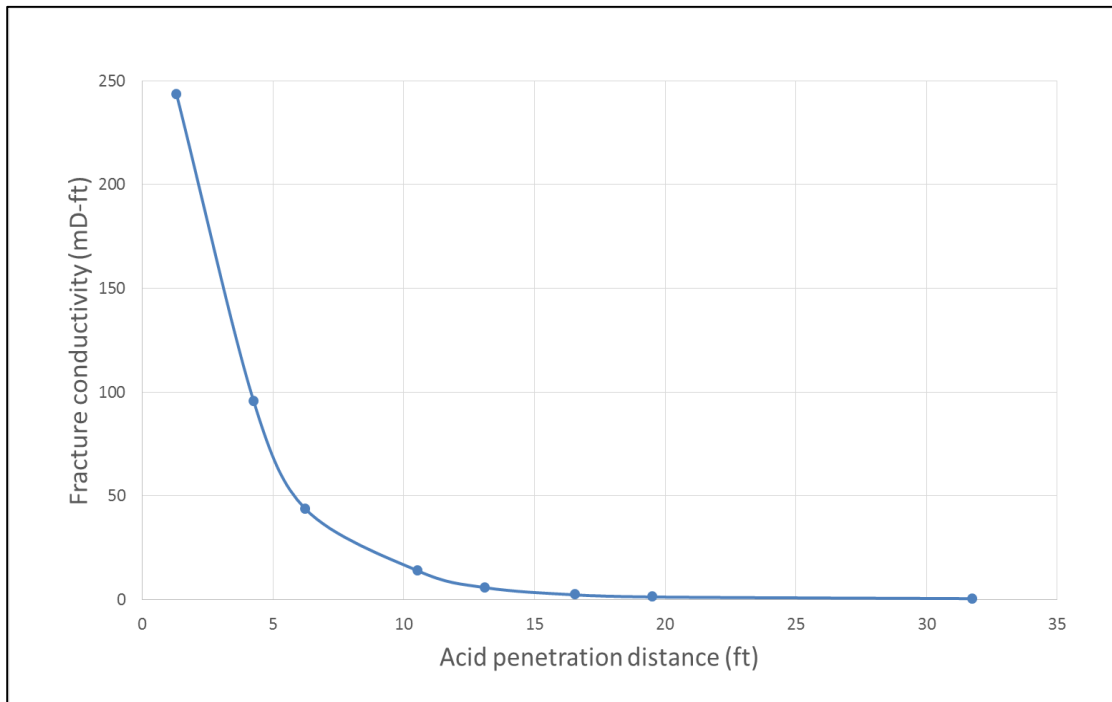
Figure 22: Fracture conductivity vs. acid penetration distance
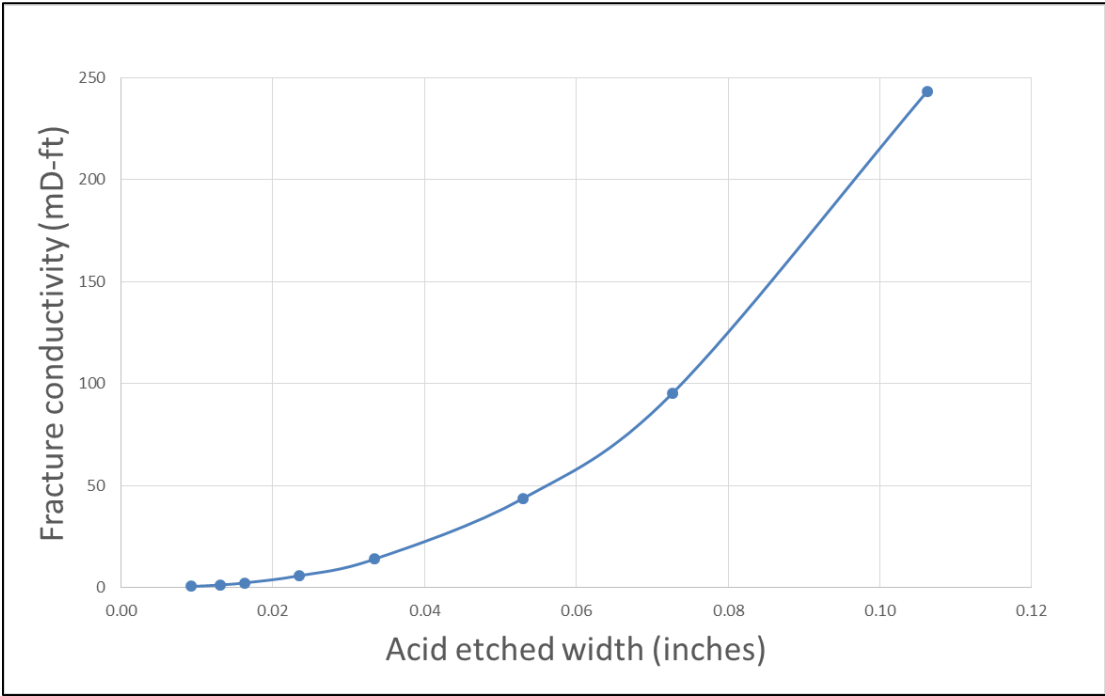
Figure 23: Fracture conductivity vs. acid-etched width
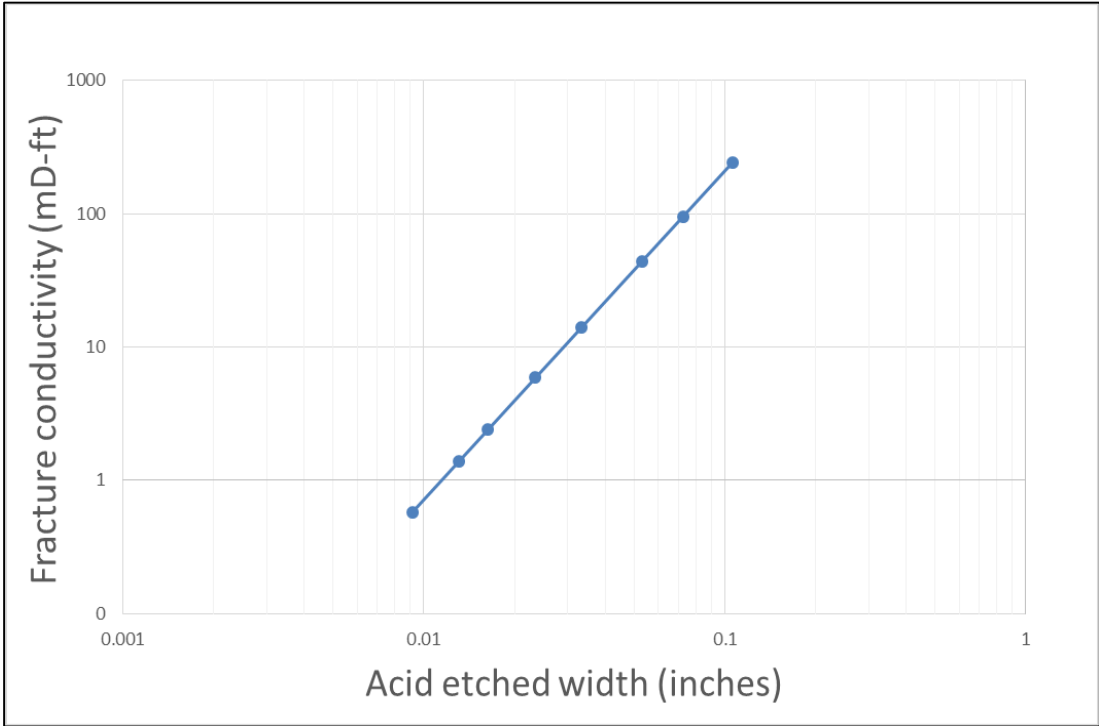
Figure 24: Fracture conductivity vs. acid-etched width log-log scale

55

Figure 25 shows the relationship between the acid-etched width and the fracture conductivity versus the acid penetration distance. Figure 25 confirms that wider etched width gives higher fracture conductivity. Furthermore, Figure 26 shows the relationship between the acid penetration distance and the fracture conductivity, and it confirms that wider width gives higher conductivity and that it happens near the fracture entrance.
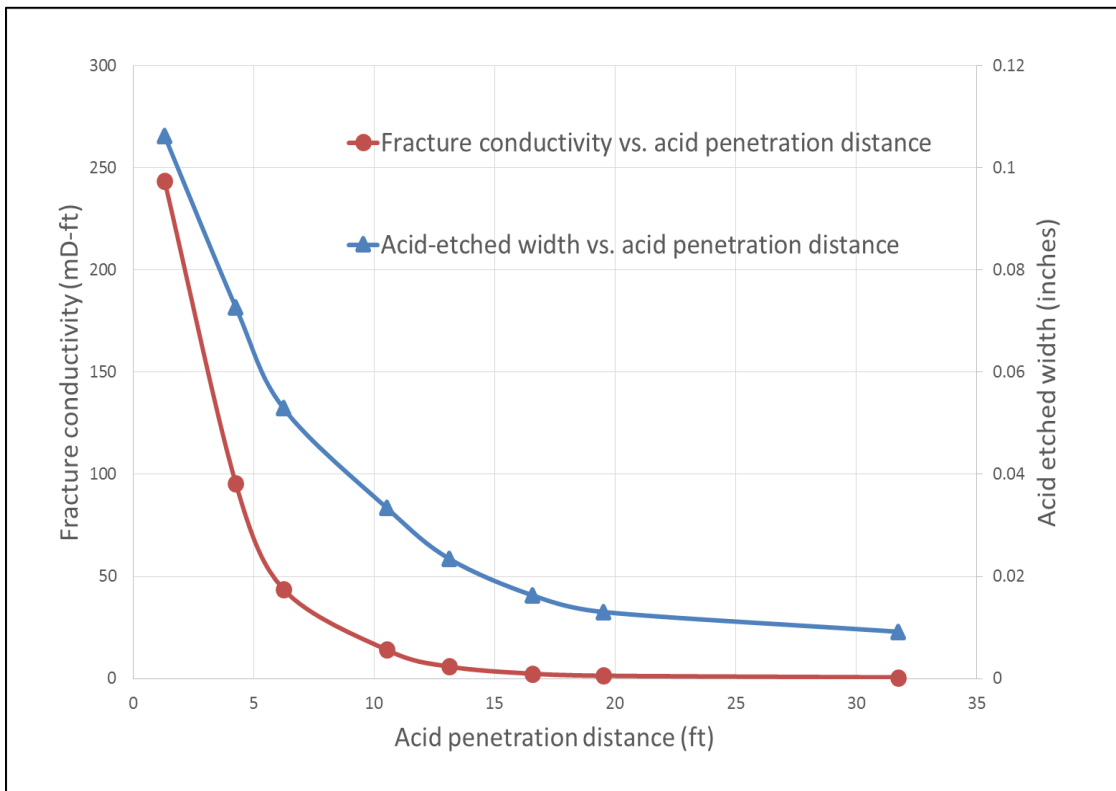
Figure 25: Comparison between acid-etched width and fracture conductivity vs. acid penetration distance
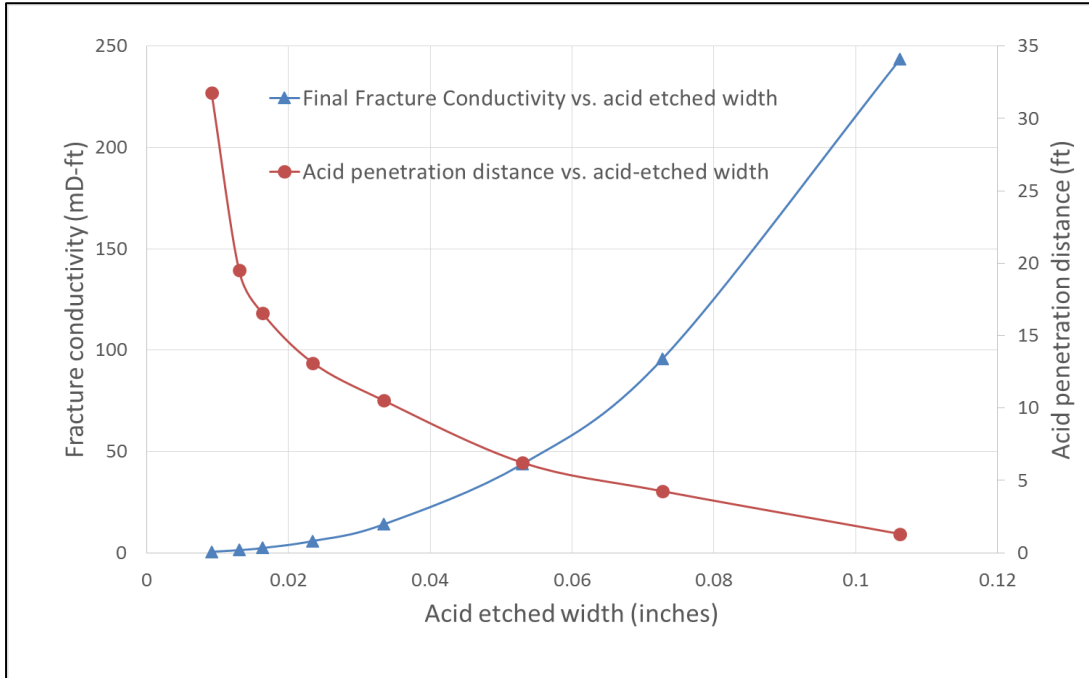
Figure 26: Comparison between acid penetration distance and fracture conductivity vs. acid-etched width

Figure 27 shows the comparison of fracture conductivity versus the acid-etched width before and after fracture closure stress is reached. The fracture conductivity after fracture closure depends on the fracture closure stress as was shown in the conductivity correlation (Eq. 26.)
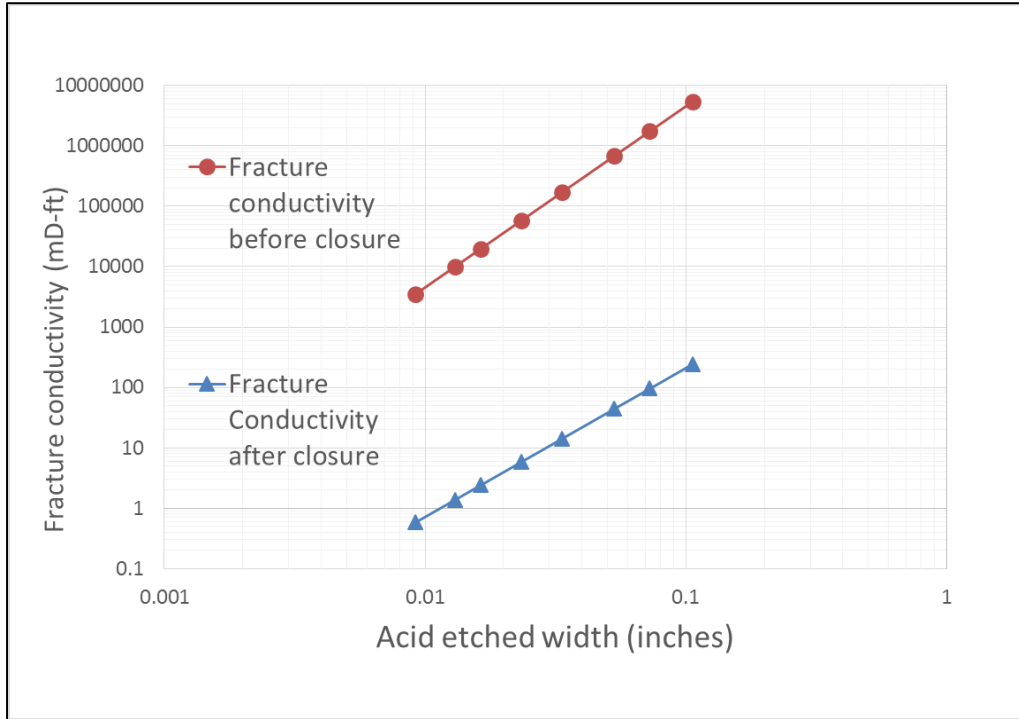
Figure 27: Fracture conductivity vs. acid-etched width – before and after fracture closure

5.4 Influence of Acid Concentration on Fracture Conductivity

To test the effect of different acid concentrations, higher acid concentration, 28% HCl, is used. Higher acid concentration means stronger acid dissolving power. Hence, when running the simulator with 15% HCl and 28% HCl for the same time steps, wider acid-etched width and longer acid penetration distance is expected to be achieved with higher HCl concentration. Figure 28 and Figure 29 show the comparison of fracture conductivity between 15% HCl and 28% HCl, and they confirm that higher acid concentration gives higher fracture conductivity for the same amount of stimulation time; yet, both concentrations give the same fracture conductivity pattern. The results are tabulated, and can be found in Appendix C.
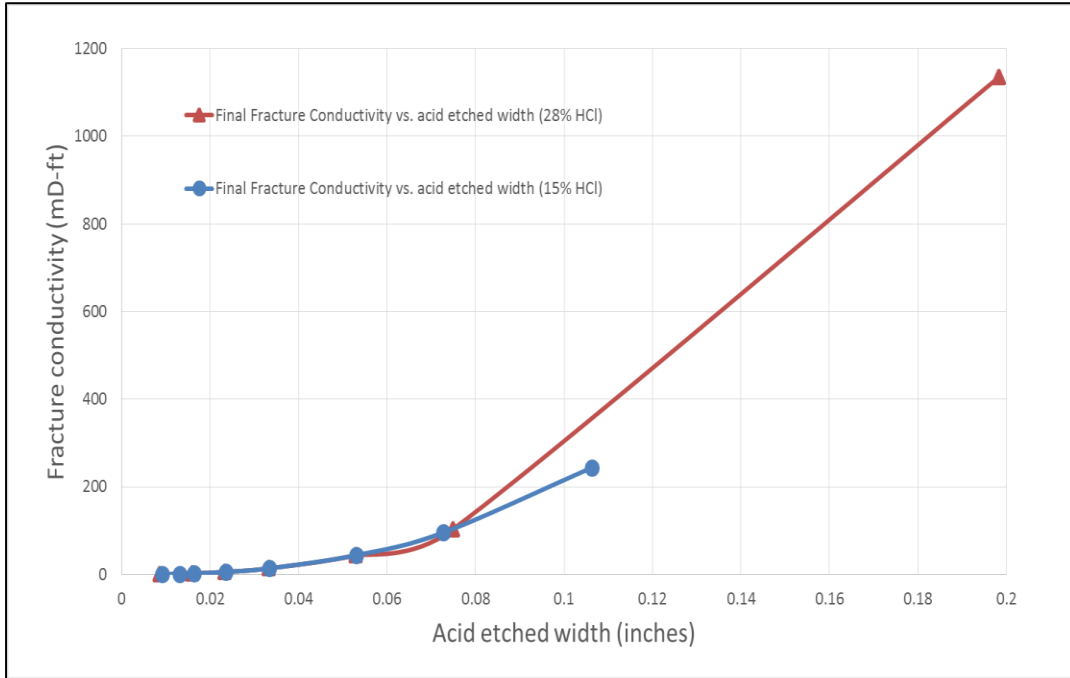
Figure 28: Comparison of 28% HCl and 15% HCl on fracture conductivity vs. acid-etched width
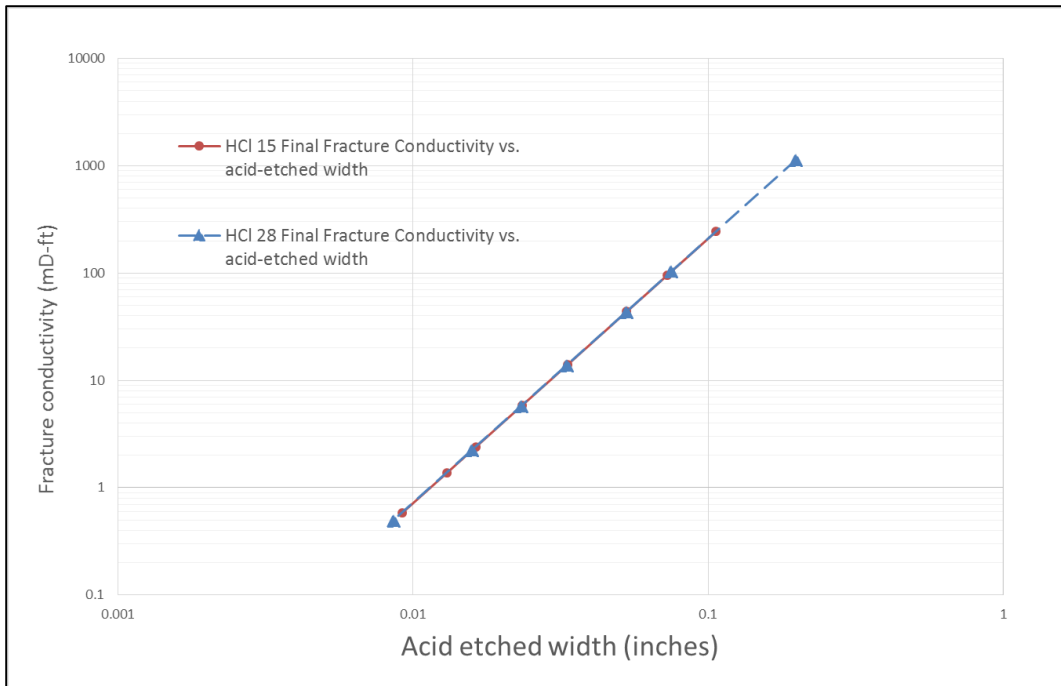
Figure 29: Comparison of 28% HCl and 15% HCl on fracture conductivity vs. acid-etched width log-log scale

5.5 Effect of Acid Diffusion along the Fracture Length

This model accounts for acid diffusion in all directions throughout the fracture and not just across the fracture width as the existing models report. To study the effect of the acid diffusion and to see how it contributes to the overall acid concentration distribution, the acid convection kernel is disabled and the comparison is shown on Figure 30 and Figure 31. Further comparisons can be found in Appendix D. It is very clear that the acid convection part dominates the diffusion part along the fracture length; however, in other cases in which the fracture is extremely small, this might not be true. Thus, the acid diffusion should be considered in all directions throughout the fracture and not just across the fracture width.
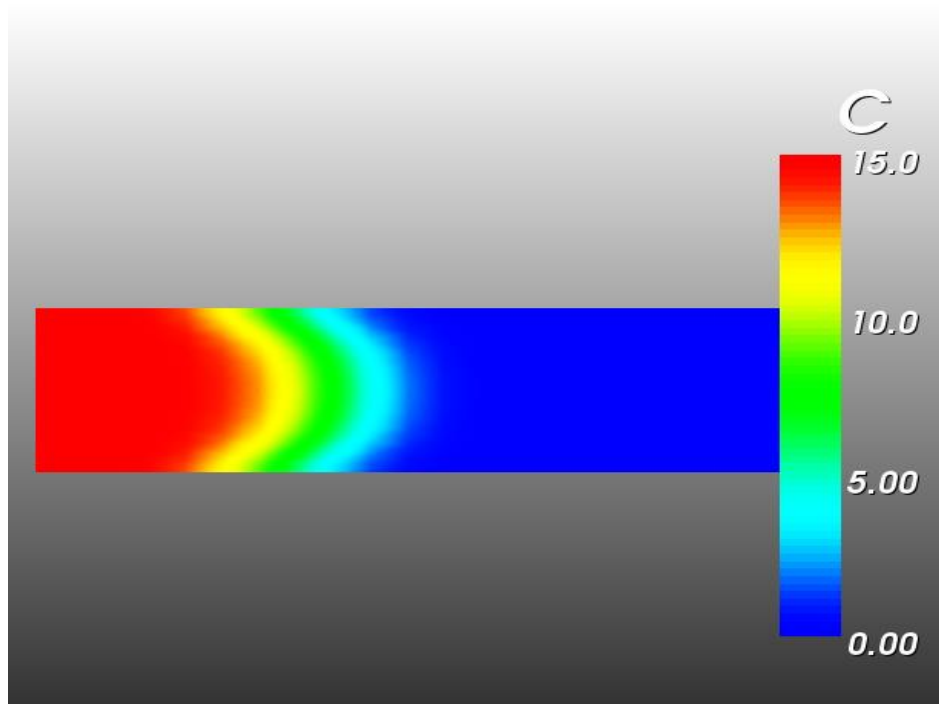
Figure 30: Acid concentration distribution and acid penetration distance due to convection, diffusion and reaction
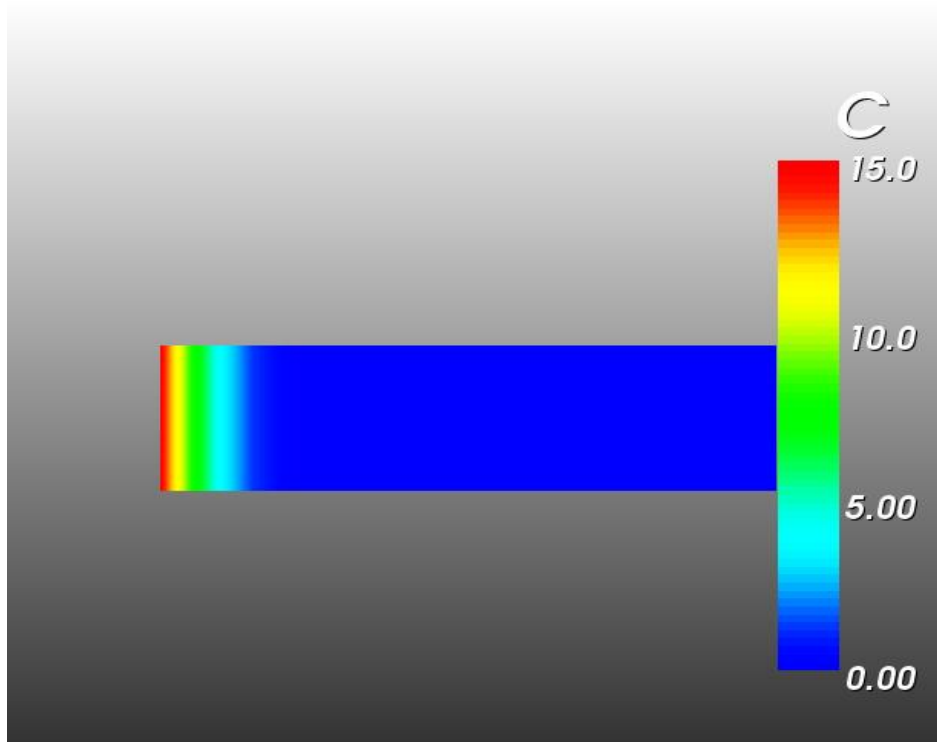
Figure 31: Acid concentration distribution and acid penetration distance due to diffusion and reaction

Chapter 6: Conclusion

6.1 Conclusion

The acid transport model that was developed using the finite element method and the weak formulation is capable of solving the complex systems of non-linear partial differential equations including the Navier-Stokes equations, the acid balance equation and the energy balance equation. The results of the numerical simulator were validated against analytical solutions to check the accuracy of the simulator. The model was found to give accurate velocity profile, temperature distribution, acid penetration distance and acid-etched width. Parametric studies were conducted to test different aspects of the acid transport model, and here are the findings:

1. Highly viscous acids, gelled acids, give longer acid penetration distance than straight acids.

2. Acids with high concentrations give longer acid penetration distance than acids with low concentrations because they have stronger dissolving power.

3. Acids with high viscosity are more preferable than acids with high concentrations because highly viscous acids tend to travel further inside the fracture before they become spent than acids with high concentrations.

4. Wide acid-etched width is achieved near the fracture entrance because the acid has its full dissolving power potential at that point; hence, as the fracture length increases the etched width decreases because the dissolving power of the acid declines.

5. The highest fracture conductivity occurs near the fracture entrance because of the wide etched-width; hence, the fracture conductivity decreases as the acid penetration distance increases.

.

Nomenclature

SI units are used for all the variables if not otherwise stated.

b = Fracture width

C, C_l, C_A = Acid concentration (%)

C_B = Acid concentration at boundary

C_c = Compressibility fluid-loss coefficient

C_{eq} = Equilibrium acid concentration

C_{wh} = Leak-off coefficient with wormholes

$C_{v,wh}$ = Viscosity fluid-loss coefficient

C_t = Total reservoir compressibility

c_p = Specific heat

D, D_{eff} = Diffusion coefficient

k_H = Thermal conductivity

f_r = Fraction of acid to react before leak-off

K = Consistency index

k = Permeability (mD)

k_{fi} = Ideal fracture permeability

k_f = Forward reaction constant

L = Length of fracture

M_w = Molecular weight

N_{pe} = Peclet number

n = Power law index

P = Pressure

P_R = Reservoir pressure

P_f = Pressure in the fracture

Q_i = Injection rate (bbl/min)

R_i = residual vector

R_e = Reynolds number

RES = rock embedment strength, which is an empirical hardness measure that correlates the fracture closer stress to its conductivity

r = Reaction rate

T = Temperature

T_R = Reservoir temperature

t = time

u, u_x= Velocity in the x-direction - (Fracture length)

u_y, v = Velocity in the y-direction - (Fracture width)

u_z = Velocity in the z-direction- (Fracture height)

v_l = Leak-off velocity

w, w_i = fracture width

wk_f = Fracture conductivity

α = Reaction order

β = Acid dissolving power

ΔH = Heat of reaction

η = Apparent viscosity

θ = Shear rate

μ = Viscosity

ρ = Acid density

σ_c = Fracture closer stress

τ = Shear stress

Φ = shape function

φ = Porosity

ψ = Test function

References

[1]   M. Brady, S. Davies, C. Fredd, D. Fu, B. Lungwitz, E. Al-Anzi, M. Al-Mutawa, N. Al-Habib, A. Al-Mumen, H. Nasr-El-Din, O. Alvarado, F. Chang, E. Huidobro, M. Jemmali, M. Samuel and D. Sandhu, "Postitive Reactions in Carbonate Reservoir Stimulation," *Oilfield Review Winter ,* 2003/2004.

[2]   B. Williams, J. Gidley and R. Schechter, Acidizing Fundamentals, New York: SPE, 1979.

[3]   J. Mou, "Modeling Acid Transport and Non-Uniform Etching in a Stochastic Domain in Acid Fracturing," Ph.D. dissertation. Texas A&M University, 2009.

[4]   M. J. Economides and K. G. Nolte, Reservoir Stimulation, Third ed., John Wiley & Sons Ltd, 2000.

[5]   M. J. Economides and K. G. Nolte, Reservoir Stimulation, Second ed., Schlumberger Educational Services, 1989.

[6]   J. Lee, "Evaluation of Acid Fracturing Using the Method of Distributed Volumtric Sources," Thesis. Texas A&M University, Texas, 2009.

[7]   "Carbonate Stimulation," *Middle East & Asia Reservoir Review. Schlumberger,* 2007.

[8]   W. Renpu, Advanced Well Completion Engineering, Third ed., Elsevier, 2011.

[9]   M. H. Lee and L. D. Roberts, "Effect of Heat Reaction on Temperature Distribution and Acid Penetration in a Fracture," SPE Journal Paper, Houston, 1980.

[10]   Settari, "Modeling of Acid-Fracturing Treatments," SPE Production & Facilities, SPE Journal Paper, 1993.

[11]   J. Donea and A. Huerta, Finite Element methods for Flow Probelms, England: WILEY, 2003.

[12]   J. N. Reddy, An Introduction to Finite Element Method, McGraw Hill, 2006.

[13]   J. N. Reddy, An Introduction to Nonlinear Finite Element Analysis, New York: OXFORD University Press, 2004.

[14]   J. Gidleu, S. Holditch, D. Nierode and R. Veatch JR., Recent Advances in Hydraulic Fracturing, Richardson TX: SPE, 1989.

[15]   H. Frasch, "Increasing the flow of oil-wells". United States Patents and Tradmark Office. Washington DC Patent 556669, 1896.

[16]   T. Perkins and L. Kern, "Widths of hydraulic fractures," Journal of Petrleum Technology, 1961.

[17]   R. Nordgren, "Propagation of a vertical hydraulic fracture," Society of Petroleum Engineering Journal, 1972.

[18]   S. Khristianovic and Y. Zheltov, "Formation of vertical fractures by means of highly viscous fluids," In Proceedings of 4th World Petroleum Congress, Vol. II, Rome, 1955.

[19]   J. Geertsma and F. Klerk., "A rapid method of predicting width and extent of hydraulic induced fractures," JPT, 1969.

[20]   T. W. Engler, "Stimulation Design Course," New Mexico Tech, 2011.

[21]   J. Adachi, E. Siebrits, A. Peirce and J. Desroches, "Computer Simulation of Hydraulic Fractures," International Journal of Rock Mechanics & Mining Sciences, 2007.

[22]   C. Yew and X. Weng, Mechanics of Hydraulic Fracturing, Waltham. MA. USA: Elsevier Inc., 2015.

[23]   J. Adachi, E. Detournay and A. Peirce, "Analysis of the classical pseudo-3D model for hydraulic fracture with equilibrium height growth across stress barriers," *International Journal of Rock Mechanics &Mining Sciences ,* pp. 625-639, 2010.

[24]   Williams and Nierode, "Design of Acid Fracturing Treatments," Journal of Petroleum Technology, SPE Journal Paper, 1972.

[25]   Roberts and Guin, "A New Method for predicting Acid Penetration Distance," SPE Journal Paper, 1975.

[26]   Lo and Dean, "Modeling of Acid Fracturing," SPE Production Engineering, SPE Journal Paper, 1989.

[27]   A. Settari, R. Sullivan and C. Hansen, "A New Two-Dimensional Model for Acid-Fracturing Design," SPE Production & Facilities, SPE Journal Paper, 2001.

[28]   J. Romero, H. Gu and S. Gulrajani, "3-D Transport in Acid-Fracturing Treatments: Theoretical Development and Consequences for Hydrocarbon Production," SPE Production & Facilities, SPE Journal Paper, 1998.

[29]   C. Oeth, "Three-Dimensional Modeling of Acid Transport And Etching in a fracture," Ph.D. dissertation. Texas A&M University, 2013.

[30]   R. B. Bird, W. E. Stewart and E. N. Lightfoot, Transport Phenomena, Second ed., John Wiley & Sons Inc, 2002.

[31]   A. Hill, D. Zhu and Y. Wang, "The Effect of Wormholing on the Fluid-Loss Coefficient in Acid Fracturing," SPE Production & Facilities, SPE Journal Paper, 1995.

[32]   D. Nierode and K. Kruk, "An Evaluation of Acid Fluid Loss Additives Retarded Acids, and Acidized Fracture Conductivity," Fall Meeting of the Society of Petroleum Engineers of AIME, 1973.

[33]   R. S. Schechter, Oil Well Stimulation, Prentice Hall, 1992.

[34]   J. Walsh, "Effect of Pore Pressure and Confining Pressure on Fracture Permeability," International Journal of Rock Mechanics and Mining Sciences & Geomechanics Abstracts, 1981.

[35]   M. Gong, "Mechanical and Hydraulic Behavior of Acid Fractures – Experimental Studies and Mathematical Modeling.," Ph.D. dissertation, The University of Texas at Austin., 1997.

[36]   J. Deng, J. Mou, A. Hill and D. Zhu, "A New Correlation of Acid-Fracture Conductivity Subject to Closure Stress," SPE Production & Operations, SPE Journal Paper, 2012.

[37]   MOOSE, "MOOSE Documentation," INL, 2016.

[38]   R. Barati and J.-T. Liang, "A review of fracturing fluid systems used for hydraulic fracturing of oil and gas wells," Appl. Polym. Sci., 131, 40735, doi: 10.1002/app.40735, 2014.

[39]   R. Barati, R. Hutchins, T. Friedel, J. Ayoub, M.-N. Dessinges and K. England, "Fracture Impact of Yield Stress and Fracture-Face Damage on

Production With a Three-Phase 2D Model," SPE production & operations. DOI: 10.2118/111457-PA, 2009.

[40]   O. C. Zienkiewicz, R. L. Taylor and P. Nithiarasu, The Finite Element Method for Fluid Dynamics, Seventh ed., U.S.: Elsevier Ltd, 2014.

[41]   K. Lund, H. S. Fogler and C. C. McCune, "Acidization-I. The Dissolution of Dolomite in Hydrochloric Acid," Great Britain, 1972.

[42]   K. Lund, H. S. Fogler, C. C. McCune and J. W. Ault, "Acidization-II The Dissolution of Calcite in Hydrochloric Acid," Great Britain, 1974.

[43]   A. Kraslawski and I. Turunen, 23 European Symposium on Computer Aided Process Engineering, First ed., Amsterdam: Elsevier, 2013.

[44]   C. Carletti, H. Grenman, C. De Blasio and T. Westerlund, "Limestone dissolution study for Wet Flue Gas Desulfurization under turbulent regimes above critical suspension speed," Amsterdam, 2013.

[45]   M. W. Conway, M. Asadi, G. S. Penny and F. Chang, "A Comparative Study of Straight/Gelled/Emulsified Hydrochloric Acid Diffusivity Coefficient Using Diaphragm Cell and Rotating Disk," Texas, 1999.

[46]   J. Stewart, Calculus, 7th ed., Belmont: Brooks Cole, 2012.

[47]   R. C. Navarrete, M. J. Miler and J. E. Gordon, "Laboratory and Theoretical Studies for Acid Fracture Stimulation Optimization," SPE Permian Basin Oil and Gas Recovery Conference, 1998.

[48]   J. Lyons, H. Nasrabadi and H. Nasr El-Din, "A Novel Model for Fracture Acidizing with Important Thermal Effects," SPE Unconventional Resources Conference, Canada, 2013.

[49]   T. Ertekin, J. H. Abou-Kassem and G. R. King, Basic Applied Reservoir Simulation, Richardson, TX. : SPE. , 2001.

[50]   K. Wu, "Numerical Modeling of Complex Hydraulic Fracture Development in Unconventional Reservoirs. Ph.D dissertation," The University of Texas at Austin, 2014.
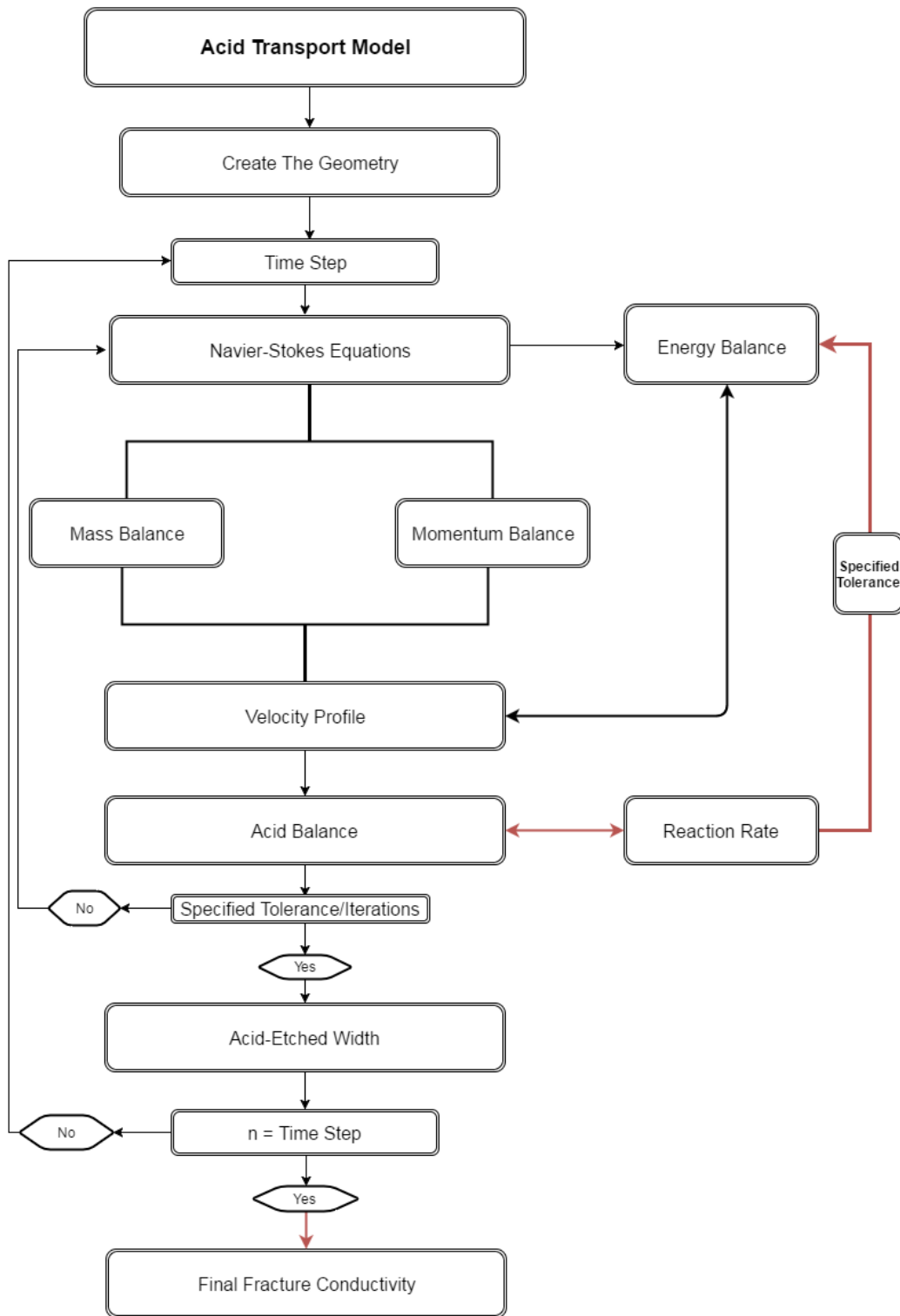
Appendix A

Figure 32: Flowchart of the Model

Appendix B

The results of the temperature validation example.

Table 10: The results of the temperature validation

Settari's model		Simulation	
Distance (m)	Temperature (degree C)	Distance (m)	Temperature (degree C)
5	65	0	65.000
10	66	10.10	71.336
13.7	68.1	20.20	76.607
14.4	70.6	30.30	80.813
15.9	72.8	40.40	83.955
17.4	75.1	50.51	86.032
21.7	79.1	60.61	87.044
26	82.1	70.71	86.992
31.1	84.5	80.81	85.875
35.3	85.8	90.91	83.693
41.7	86.5	101.01	80.680
48.8	87.3	111.11	79.303
58	86.3	121.21	77.936
67.9	85.3	131.31	76.578
71.4	84.3	141.41	75.229
77.1	83.3	151.52	73.890
83.4	82.1	161.62	72.561
88.4	81.3	171.72	71.241
94.7	80	181.82	69.930
102	78.5	191.92	68.630
107	77.5	202.02	67.472
113	76.5	212.12	66.897
122	75	222.22	66.395
130	73.6	232.32	65.966
136	72.8	242.42	65.610
145	71.8	252.53	65.610
153	70.6	262.63	65.610
165	69.8	272.73	65.610
175	68.8	282.83	65.610
184	68.1	292.93	65.610
199	67.6	303.03	65.610
211	67.3	313.13	65.610
228	66.9	323.23	65.610
242	66.8	333.33	65.610
260	66.4	343.43	65.610
274	66.1		
300	66.1		
330	66.1		
340	66.1		

Appendix C

Table 11 and Table 12 represent the data used to plot the figures for the fracture conductivity test with acid concentration of 15%.

Table 11: The data for 15% HCl fracture conductivity test

stimulation time (s)	Penetration distance (m)	Etched width (in)	RES (pa)	σ (pa)
30	0.4	0.10625	3.1E+08	47200000
60	1.3	0.07270	3.1E+08	47200000
120	1.9	0.05301	3.1E+08	47200000
300	3.21	0.03341	3.1E+08	47200000
600	4	0.02347	3.1E+08	47200000
1200	5.05	0.01632	3.1E+08	47200000
1800	5.95	0.01305	3.1E+08	47200000
3600	9.68	0.00917	3.1E+08	47200000

Table 12: The result for 15% HCl fracture conductivity test

Ideal fracture conductivity before closure (mD-ft)	C1	C2	Fracture conductivity (m^3)	Final Fracture conductivity after closure (mD-ft)
5444621.02	1.76387E-11	1.16185E-07	7.32513E-14	243.516
1744162.85	6.91966E-12	1.16185E-07	2.87365E-14	95.531
676406.92	3.17637E-12	1.16185E-07	1.31911E-14	43.852
169290.37	1.01727E-12	1.16185E-07	4.2246E-15	14.044
58691.81	4.25864E-13	1.16185E-07	1.76856E-15	5.879
19738.09	1.73877E-13	1.16185E-07	7.22089E-16	2.401
10084.47	1.00116E-13	1.16185E-07	4.15769E-16	1.382
3504.28	4.19914E-14	1.16185E-07	1.74385E-16	0.580

Table 13 and Table 14 represent the data used to plot the figures for the fracture conductivity test with acid concentration of 28%.

Table 13: The data for 28% HCl fracture conductivity test

Stimulation time (s)	Penetration distance (m)	Etched width (in)	RES (pa)	σ (pa)
10	1.3	0.34376	3.10E+08	4.72E+07
30	2.4	0.19837	3.10E+08	4.72E+07
60	3.3	0.07493	3.10E+08	4.72E+07
120	3.8	0.05288	3.10E+08	4.72E+07
300	4.4	0.03322	3.10E+08	4.72E+07
600	5.2	0.02322	3.10E+08	4.72E+07
1200	6.2	0.01588	3.10E+08	4.72E+07
3000	8.1	0.00859	3.10E+08	4.72E+07

Table 14: The result for 28% HCl fracture conductivity test

C1	C2	Fracture conductivity (m^3)	Final Fracture conductivity after closure (mD-ft)
3.19E-10	1.16185E-07	1.33E-12	4406.030
8.23E-11	1.16185E-07	3.42E-13	1135.558
7.46E-12	1.16185E-07	3.10E-14	102.938
3.16E-12	1.16185E-07	1.31E-14	43.570
1.00E-12	1.16185E-07	4.17E-15	13.850
4.15E-13	1.16185E-07	1.72E-15	5.728
1.63E-13	1.16185E-07	6.75E-16	2.244
3.57E-14	1.16185E-07	1.48E-16	0.492

Appendix D

Sample data and results.

Table 15: Geometry Properties

Fracture Geometry Properties			
Length (m)	Width (mm)	Number of elements	Number of global nodes
10	2	100	441

Table 16: Sample of input data

Input parameters	Value	Unit
Injection rate	7.55	bbl/min
Viscosity	1	pa-s
Density	1000	kg/m^3
Thermal conductivity	0.584	Watts/m-C
Specific heat	4.179	KJoule/Kg-C
Diffusivity coefficient	0.0001	m^2/s
Temperature Reference	60	ºC
Reaction order	1	
Reaction constant	0.000688	cm/s
Heat of reaction	1.09E+03	KJoule/Kg
Initial acid concentration	15	%
Leak-off Coefficient	0.0006	m/$\sqrt{s}$

Table 17: Results of the sample data

Stimulation Time (minutes)	Total injected volume (bbl)	Total leak-off volume (bbl)
5	37.75	7.5
10	75.5	15
60	453	90

Validation of acid balance equation and acid-etched width equation

Table 18: Simulation & analytical validation of acid balance equation

Validation of acid balance equation	
Dimensionless penetration (simulation)	0.9680
Dimensionless penetration (Analytical)	0.9650
Dimensionless average concentration (simulation)	0.3787
Dimensionless average concentration (Analytical)	0.3780

Table 19: Validation of acid-etched width - without leak-off

Validation of acid-etched width equation	
Acid-etched width (mm) (Simulation – without leak-off)	0.2338
Acid-etched width (mm) (Analytical)	0.2330

Table 20: Validation of acid-etched width - with leak-off

Validation of acid-etched width equation	
Acid-etched width (mm) (Simulation – With leak-off)	0.2140
Acid-etched width (mm) (Analytical)	0.2330

Parts of the input file are shown in Figure 33.

```
[Variables]
  # x-velocity
  [./u]
    order = SECOND
    family = LAGRANGE
  [../]
  # y-velocity
  [./v]
    order = SECOND
    family = LAGRANGE
  [../]
  # Temperature
  [./T]
    order = SECOND
    family = LAGRANGE
  [../]
  # Acid
  [./C]
    order = SECOND
    family = LAGRANGE
  [../]
  # Pressure
  [./p]
    order = FIRST
    family = LAGRANGE
  [../]
[]
[BCs]
  [./leakoff]
    type = FunctionDirichletBC
    variable = u
    boundary = 'bottom'
    function = leakoff
  [../]
  [./inlet]
    type = DirichletBC
    variable = u
    boundary = 'left'
    value = 0.001 # (m/s) )
  [../]
```

Figure 33: Part of the input file

Parts of the C++ code file for the acid balance equation are shown in Figure 34.

```cpp
template<>
InputParameters validParams<Acid>()
{
  InputParameters params = validParams<Kernel>();
  // Coupled variables
  params.addRequiredCoupledVar("u", "x-velocity");
  params.addCoupledVar("v", "y-velocity"); // only required in 2D and 3D
  params.addCoupledVar("w", "z-velocity"); // only required in 3D
  // Required parameters
  params.addRequiredParam<Real>("D", "AcidDiffusivity");
  return params;
}
Acid::Acid(const InputParameters & parameters) :
  Kernel(parameters),
  // Coupled variables
  _u_vel(coupledValue("u")),
  _v_vel(_mesh.dimension() >= 2 ? coupledValue("v") : _zero),
  _w_vel(_mesh.dimension() == 3 ? coupledValue("w") : _zero),
  // Variable numberings
  _u_vel_var_number(coupled("u")),
  _v_vel_var_number(_mesh.dimension() >= 2 ? coupled("v") : libMesh::invalid_uint),
  _w_vel_var_number(_mesh.dimension() == 3 ? coupled("w") : libMesh::invalid_uint),
  // Required parameters
  _D(getParam<Real>("D"))
{
}
Real Acid::computeQpResidual()
{
  // The convection part,  u.grad(C) * v.
  // _u is the acid concentration variable, _grad_u is its gradient.
  Real convective_part =
    (_u_vel[_qp]*_grad_u[_qp](0) +
     _v_vel[_qp]*_grad_u[_qp](1) +
     _w_vel[_qp]*_grad_u[_qp](2)) * _test[_i][_qp];
  // Acid diffusion part, D * grad(C) * grad(v)
  Real diffusion_part = _D * _grad_u[_qp] * _grad_test[_i][_qp];
  return convective_part + diffusion_part;
}
Real Acid::computeQpJacobian()
{
  RealVectorValue U(_u_vel[_qp], _v_vel[_qp], _w_vel[_qp]);
  Real convective_part =  (U * _grad_phi[_j][_qp]) * _test[_i][_qp];
  Real diffusion_part = _D * (_grad_phi[_j][_qp] * _grad_test[_i][_qp]);
  return convective_part + diffusion_part;
}
Real Acid::computeQpOffDiagJacobian(unsigned jvar)
{
  if (jvar == _u_vel_var_number)
  {
    Real convective_part = _phi[_j][_qp] * _grad_u[_qp](0) * _test[_i][_qp];
    return convective_part;
  }
  else if (jvar == _v_vel_var_number)
  {
```

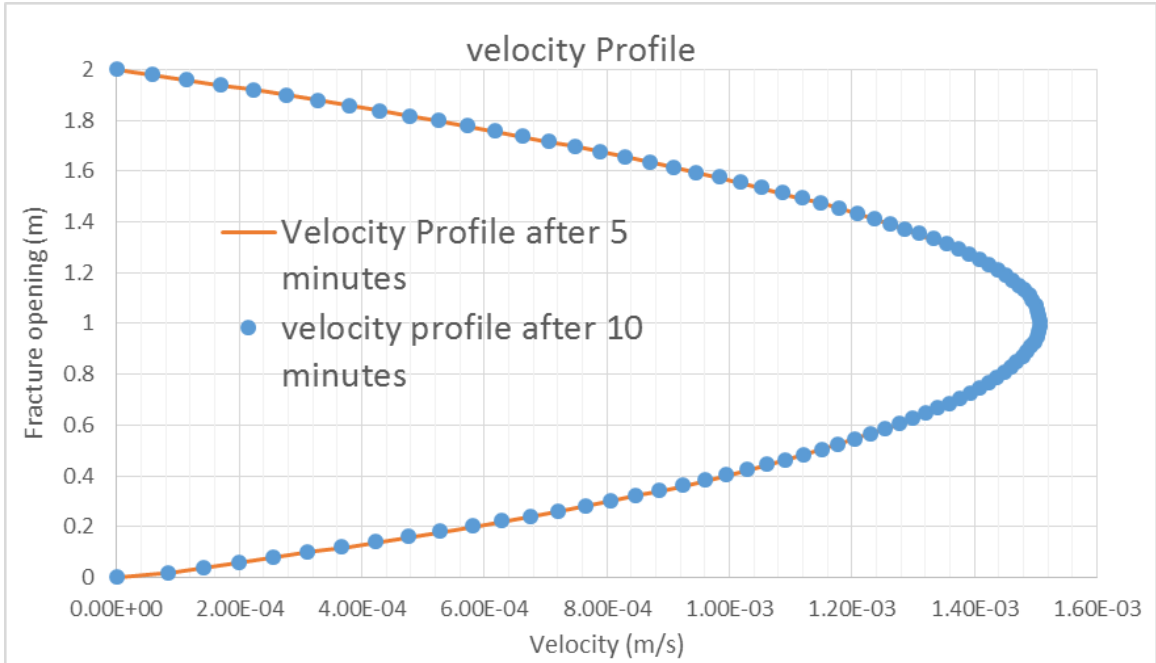*Figure 34: Part of the C++ code of the acid balance equation*

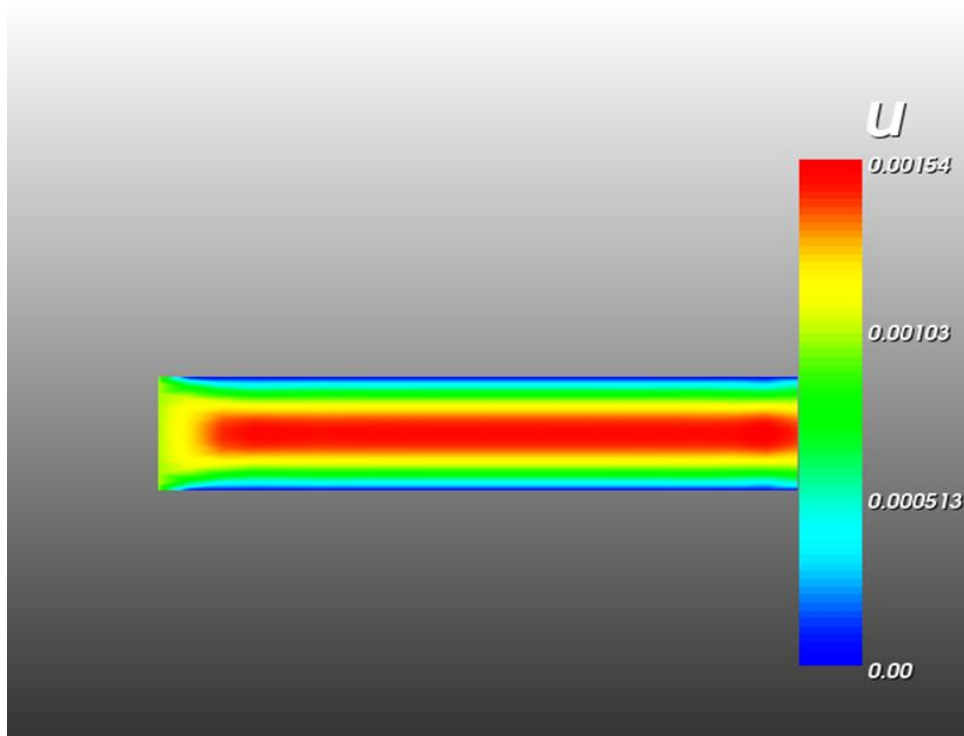*Figure 35: Velocity profile inside the fracture*

Figure 36: Velocity profile inside the fracture after 10 minutes of stimulation

Comparison between the effect of convection and diffusion on the acid concentration distribution.
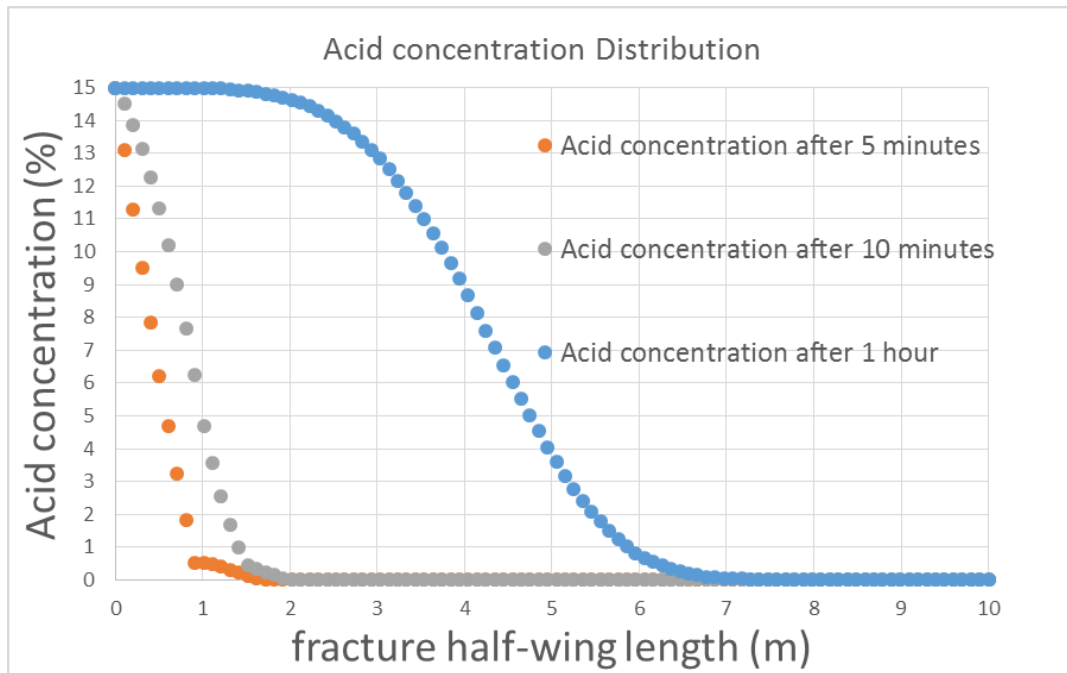

Figure 37: Acid concentration distribution inside the fracture (convection, diffusion & reaction)
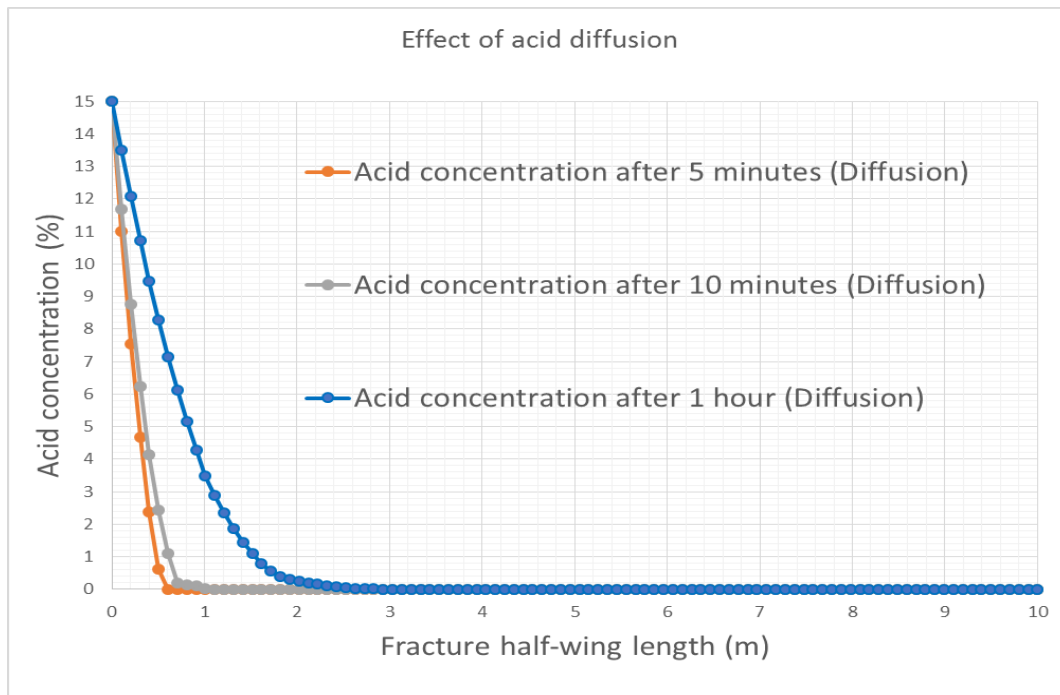

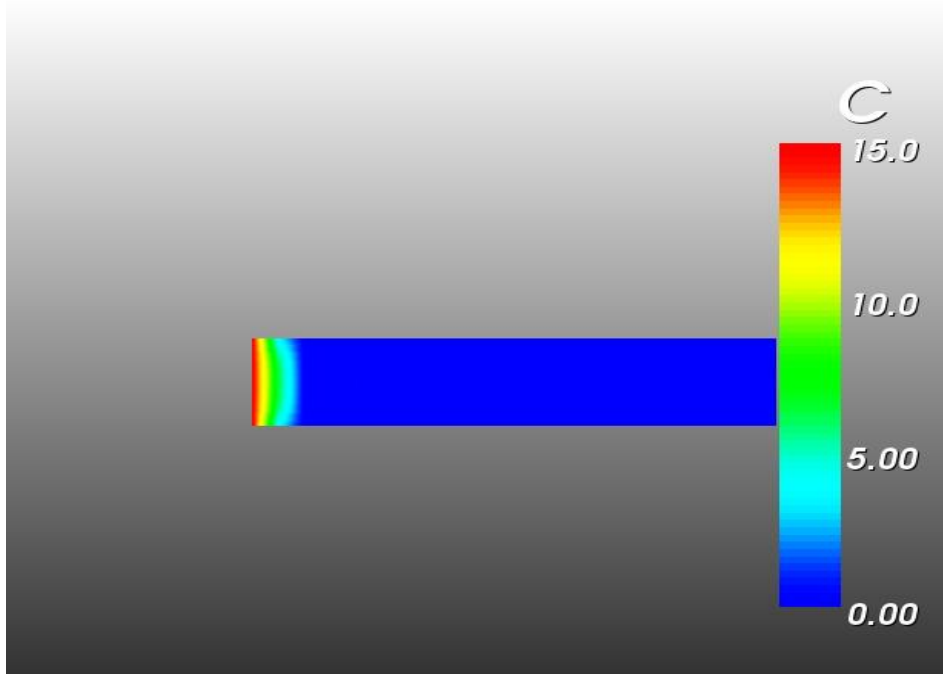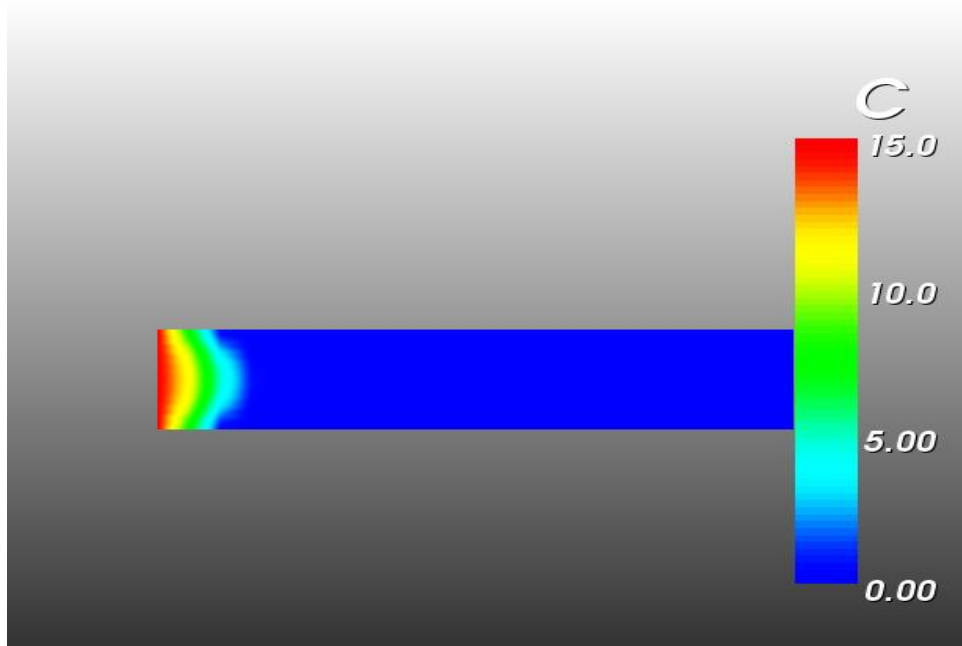*Figure 38: Acid concentration distribution due to diffusion and reaction inside the fracture*

Figure 39: Acid concentration distribution after 5 minutes of stimulation (convection, diffusion & reaction)
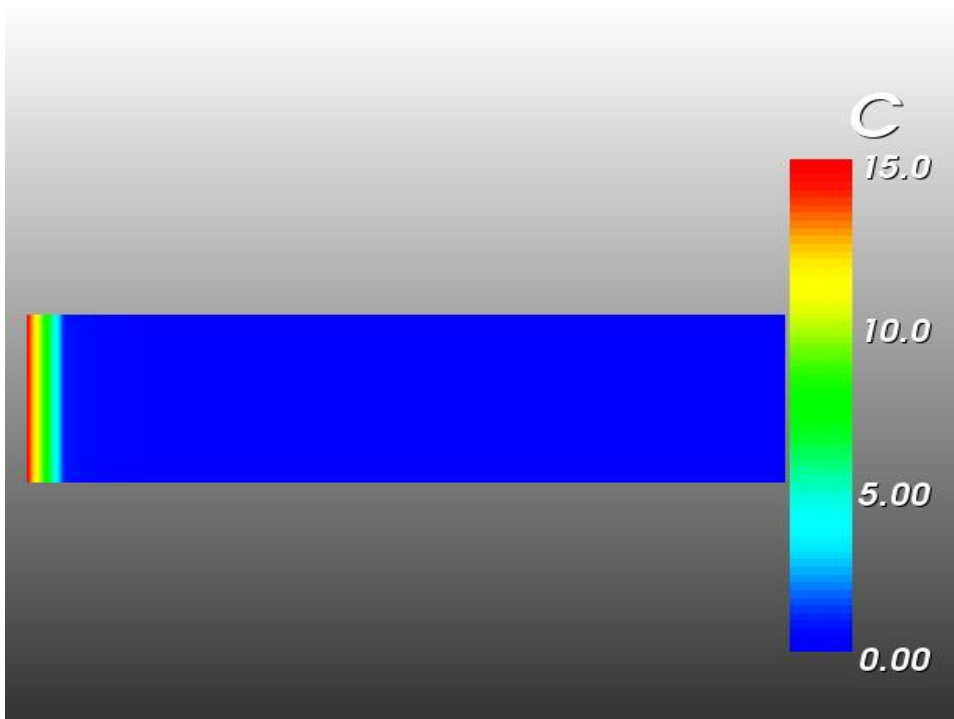
Figure 40: Effect of acid diffusion and reaction on acid concentration distribution after 5 minutes of stimulation

Figure 41: Acid concentration distribution after 10 minutes of stimulation (convection, diffusion & reaction)
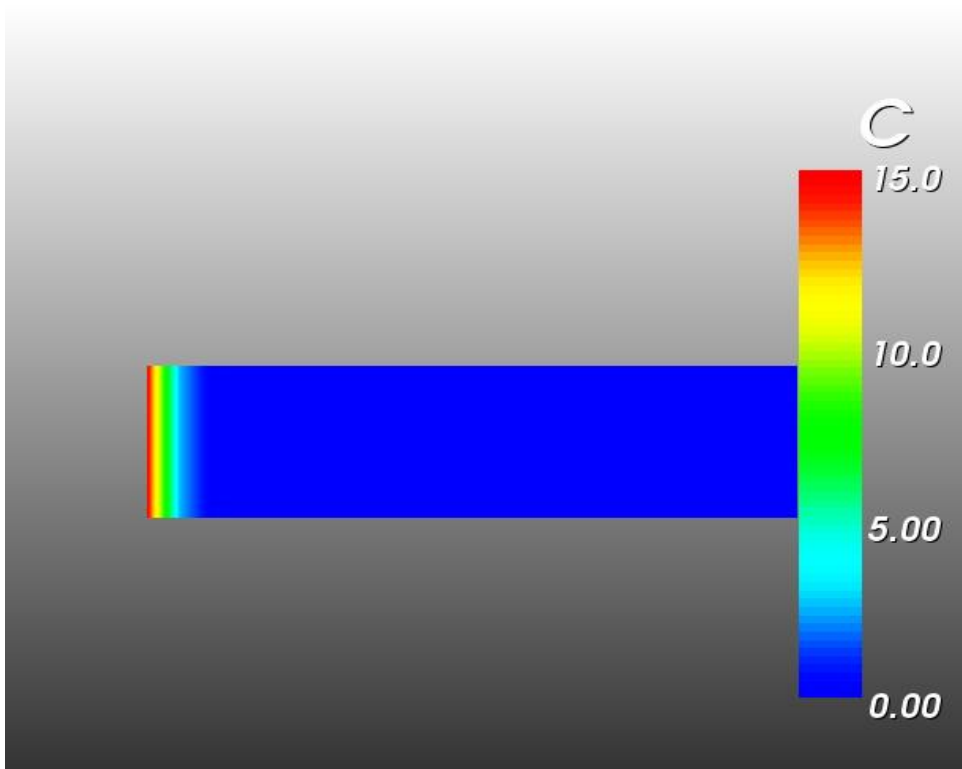

Figure 42: Effect of acid diffusion and reaction on acid concentration distribution after 10 minutes of stimulation
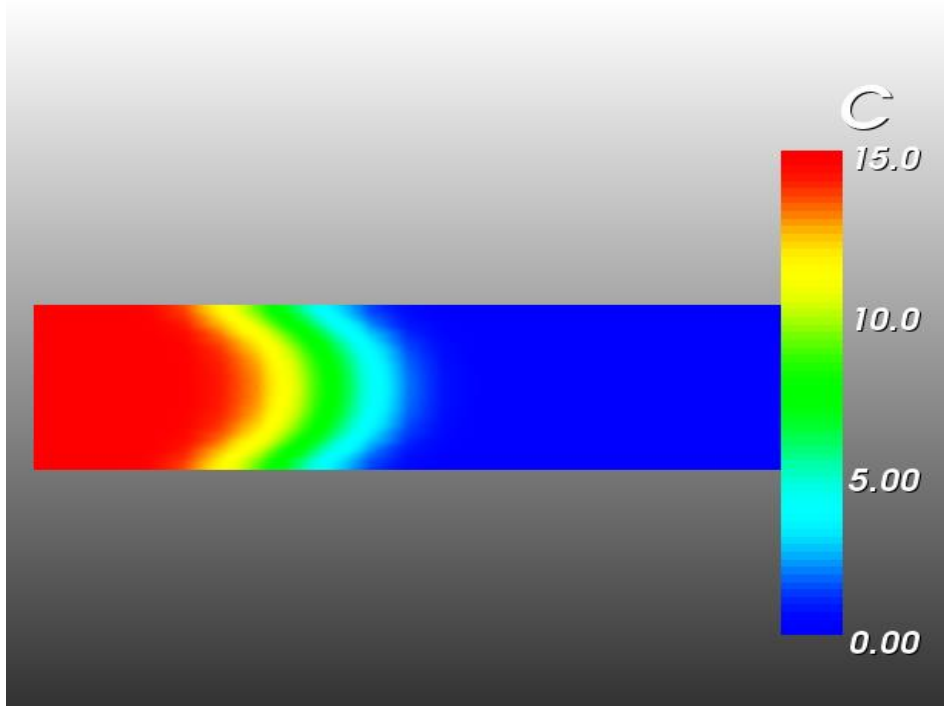
Figure 43: Acid concentration distribution after 1 hour of stimulation (convection, diffusion & reaction)
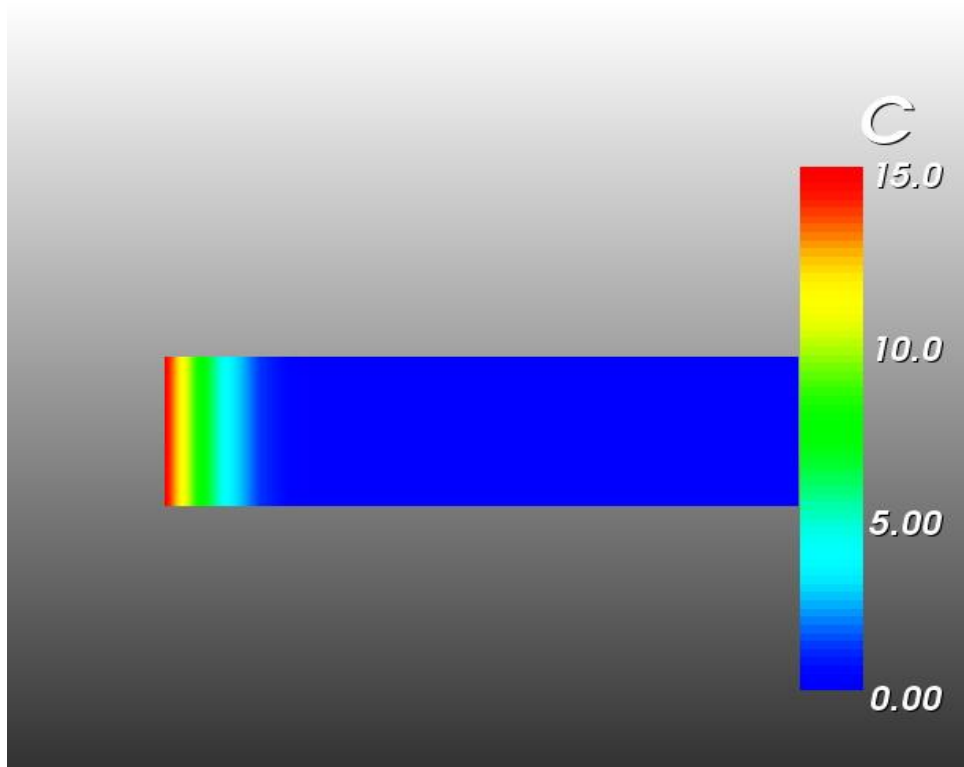

Figure 44: Effect of acid diffusion and reaction on acid concentration distribution after 1 hour of stimulation